12-2017

An Observational and Modeling Study of Mesoscale Airmasses with High Theta-e

Lawrence Wolfgang Hanft
University of Nebraska-Lincoln, wolfganghanft@huskers.unl.edu

Hanft, Lawrence Wolfgang, "An Observational and Modeling Study of Mesoscale Airmasses with High Theta-e" (2017). *Dissertations & Theses in Earth and Atmospheric Sciences*. 96.
http://digitalcommons.unl.edu/geoscidiss/96

AN OBSERVATIONAL AND MODELING STUDY OF MESOSCALE AIR MASSES WITH HIGH THETA-E

by

Lawrence Wolfgang Hanft

A THESIS

Presented to the Faculty of
The Graduate College at the University of Nebraska
In Partial Fulfillment of Requirements
For the Degree of Master of Science

Major: Earth and Atmospheric Sciences

Under the Supervision of Professor Adam L. Houston

Lincoln, Nebraska

December, 2017

AN OBSERVATIONAL AND MODELING STUDY OF MESOSCALE AIR MASSES WITH HIGH THETA-E

Lawrence Wolfgang Hanft, M.S.

University of Nebraska, 2017

Adviser: Adam L. Houston

Typically, the cool side of an airmass boundary is stable to vertical motions due to its associated negative buoyancy. However, under certain conditions, the air on the cool side of the boundary can undergo a transition wherein it assumes an equivalent potential temperature and surface-based convective available potential energy that is higher than that of the airmass on the warm side of the boundary. The resultant airmass is herein referred to as a mesoscale airmass with high theta-e (MAHTE).

Results are presented from an observational and mesoscale modeling study designed to examine MAHTE characteristics and the processes responsible for MATHE formation and evolution. Observational analysis focuses on near-surface observations of a MAHTE in northwestern Kansas on 20 June 2016 collected through multiple transects executed with an Integrated Mesonet and Tracker. The highest equivalent potential temperature is found to be 15 – 20 K higher than what was observed in the warm sector and located 2 – 5 km on the cool side of the boundary. This case was modeled using WRF-ARW to examine the processes involved in MAHTE formation that could not be inferred through observations alone. Simulations faithfully reproduce many characteristics of the observed MAHTE. Model analysis indicates that differential vertical advection of equivalent potential temperature across the boundary is important for simulated MAHTE formation. Specifically, deeper vertical mixing/advection in the warm sector reduces moisture (equivalent potential temperature), while vertical motion/mixing is suppressed on the cool side of the boundary thereby allowing largely unmitigated diurnally-driven increases in equivalent potential temperature. Model analysis also suggests that surface fluxes did not play a major direct role in MAHTE formation.

Acknowledgments

I would like to thank my advisor Dr. Adam Houston, as well as my committee members Drs. Matthew Van Den Broeke and Clint Rowe for all of their guidance and support with this project. I would also like to thank Dr. George Limpert for his assistance with setting up and running the WRF model, as well as Curtis Riganti for his help with code used for analysis. I would also like to thank the other members of the Severe Storms Research Group, both past and present, for numerous helpful discussions, and for their help with collecting data used in this project. Lastly, I would like to thank my friends and family for all their continued support and encouragement throughout the completion of this work.

This work was made possible through the National Science Foundation grants AGS-1542760 and OIA-1539070.

Table of Contents

List of Figures

List of Tables

Chapter 1

Introduction

Thunderstorm outflow is typically colder and thus more gravitationally stable than the ambient environment. However, there are cases where a thin area along the leading edge of the outflow air mass can have higher conditional instability (and thus, higher convective available potential energy, CAPE) due to higher equivalent potential temperature. This localized area will be referred to as a Mesoscale Air mass with High Theta-E, or MAHTE. MAHTEs are typically 10-20 km in width (Rasmussen et al. 2000; Gilmore and Wicker 2002), and may extend along significant lengths of synoptic boundaries; however the limited observations available are insufficient to reveal the exact lengths of MAHTEs. Forecasting their development is complicated because most forecasting models cannot resolve them, and because the processes responsible for their formation are not fully understood; thus, conceptual models and forecasting heuristics have not been developed. This study aims to address the characterized MAHTE structure using data collected within a MAHTE, and examine the possible mechanisms for MAHTE formation through mesoscale modeling.

Although convection may not initiate in these thin areas of higher conditional instability, they could potentially influence any convection that forms along the boundary and interacts with the MAHTE. A notable example was the Aurora, Nebraska, supercell on 22 June 2003 (Guyer and Ewald 2004). Overnight on the 21st-22nd, thunderstorms produced an outflow boundary which was positioned north-south across central

Nebraska. As an upper-level trough approached the region from the west, storms initiated in the warm sector adjacent to the outflow boundary where confluence was observed (Guyer and Ewald 2004). Prior to thunderstorm initiation, the outflow boundary showed characteristics of a MAHTE. Guyer and Ewald (2004) found the highest values of θ_e were located at the leading edge of the outflow, which they attributed to the combination of "moisture pooling" on the cool side of the boundary and insolation across the entire region. As storms crossed the boundary, rapid intensification was observed potentially as a result of the increased CAPE of 500 to 1000 J kg^{-1} (Guyer and Ewald 2004; Wakimoto et al. 2004). The storm which passed near Aurora, NE, produced a record-breaking seven inch hailstone.

Another well documented case of a MAHTE occurred on 2 June 1995. During the morning, storms in the northern Texas panhandle produced a southward-advancing outflow boundary. By the afternoon, mobile mesonets associated with the Verification of the Origins of Rotation in Tornadoes EXperiment (VORTEX) (Rasmussen et al. 1994) transected this boundary and recorded a localized increase in water vapor mixing ratio directly on the cool side of the outflow boundary (Rasmussen et al. 2000). Soundings taken on each side of the boundary suggested that vertical mixing was occurring through greater depths on the warm side of the boundary than on the cool side (Gilmore and Wicker 2002). The cause of the higher water vapor mixing ratio directly along the cool side of the boundary was not known; however, shallower mixing in the outflow air mass would allow for less dry air entrainment into the cold pool compared to the environmental air mass. This would allow water vapor mixing ratios to remain higher in the outflow air mass. Slightly lower temperatures and increased water vapor mixing ratios resulted in the outflow air mass directly on the cool side of the boundary having a higher θ_e than the air in the warm sector (Rasmussen et al. 2000). Storms in the afternoon initiated in the warm sector, rapidly strengthened after moving across the boundary, and produced several significant tornadoes (Rasmussen et al. 2000).

MAHTEs can also form along warm fronts (e.g., Groenemijer et al. 2011). An example of this occurred on the cool side of a warm front that was positioned over central England on 28 July 2005. Dewpoint temperatures directly on the cool side of the warm front were higher than those observed in the warm air mass. Despite lower temperatures, this resulted in a localized maximum in θ_e and CAPE directly on the cool side of the warm front. Groenemijer et al. (2011) hypothesized that the difference in dewpoint temperatures, and thus differences in θ_e, were caused by differences in insolation and mixing on either side of the boundary. Clearing south of the warm front resulted in deeper convective mixing which reduced dewpoint temperatures in the warm air mass. Cloud cover remained along and north of the warm front into the afternoon, reducing insolation and therefore reducing the vertical depth of convective mixing north of the warm front. Groenemijer et al. (2011) speculate that this, combined with an easterly wind off the ocean, kept dewpoint temperatures high and resulted in the formation of a MAHTE by the afternoon.

From these cases, it is evident that MAHTEs can pose a significant risk for increased severity in thunderstorms with which they interact. Due to the small width of MAHTEs, on the order of meso-γ, current operational models are not able to adequately resolve their formation. It is important to understand the characteristics of MAHTEs, as well as the processes responsible for their formation in order for forecasters to predict when thunderstorm outflow will undergo this transition into a MAHTE so as to properly assess the potential for severe weather in a localized area.

Chapter 2

Background

Changes in θ_e that ultimately lead to MAHTE formation can be described through the rate of change of entropy. Entropy is a thermodynamic state variable which describes the amount of available energy that can be converted into mechanical work. It is given by

$$s = \left(c_{pd} + r_t c_l\right) ln(T) - R_d ln(p_d) + \frac{L_v r}{T} - r R_v ln(H),$$

where s is entropy, c_{pd} is the heat capacity of dry air at constant pressure, r_t is the total water mixing ratio, c_l is the heat capacity of liquid water, T is the temperature, R_d is the gas constant of dry air, p_d is the partial pressure of dry air, L_v is the latent heat of vaporization of water, r is the mixing ratio, R_v is the gas constant for water vapor, and H is the relative humidity (Emanuel 1994). Entropy is directly related to equivalent potential temperature through

$$\left(c_{pd} + r_t c_l\right) ln(\theta_e) \stackrel{\text{def}}{=} s + R_d ln(p_0),$$

where θ_e is the equivalent potential temperature, R_d is the gas constant for dry air, and p_0 is a reference pressure (Emanuel 1994). Entropy, and thus θ_e, is a function of temperature, pressure, and the mass concentrations of water vapor (Hauf and Holler 1987). In the atmosphere, the most important quantity of mass is water in all its various phases. Entropy and θ_e are typically conserved in the absence of irreversible processes. The most dominant of these irreversible processes that result in an increase in entropy is diabatic heating at constant pressure, primarily through increased heat fluxes driven by insolation (Peixoto et al. 1991; Goody 2000; Raymond 2013). After diabatic processes, increases in entropy due to irreversible processes are dominated by phase transitions of water (Pauluius and Held 2002). This includes the evaporation of rain in unsaturated air (Emanuel 1994), non-equilibrium phase changes, and evaporation from either a body of water or land surface where the heat capacity of the storage term is large enough that energy for evaporation is drawn from the body of water or land surface, rather than being removed from the atmosphere (Emanuel 1994; Raymond 2013). For evaporation to result in an increase in entropy, the temperature at which this phase transition occurs is important. Evaporation occurring at warmer temperatures, i.e. temperatures comparable to those typically at cloud base or in the boundary layer, results in a entropy increase, while evaporation at colder temperatures like those found at cloud tops do not (Banno 2002; Pauluis and Held 2002). Other irreversible processes which can result in an increase in entropy include the diffusion of water vapor into the system, frictional dissipation, and molecular diffusion (Peixoto et al. 1991; Raymond 2013). Most of these processes either result in an increase in temperature of the system, or result in an increase of mass and therefore an increase in entropy (Raymond 2013). Because equivalent potential temperature is derived from entropy, any increase in entropy will result in an increase in equivalent potential temperature. These irreversible changes to entropy would apply to changes of entropy observed in both a Lagrangian and Eulerian frame of reference. In an Eulerian frame of reference, one would also have to also include the advection of θ_e and advection of variables which could change θ_e over time. This includes the advection of moisture and temperature.

Laboratory studies have shown that cold pools can be treated as atmospheric density currents (Charba 1974; Simpson 1987). Some of these studies have illustrated that the head of the density current remains relatively undiluted throughout the duration of the cold pool life cycle (Lowe et al. 2002). The highest wind speeds at the surface within a density current were found to be directly behind the cold pool head and underneath the dissipative wake, with average wind speed in this region 30% to 50% higher than the velocity of the density current (Figure 2.1; Lowe et al. 2002). Within the cold pool head, observed wind velocities are approximately 10% higher than the speed of the density current (Lowe et al. 2002), resulting in the formation of an internal circulation in the density current head (Robinson et al. 2013).

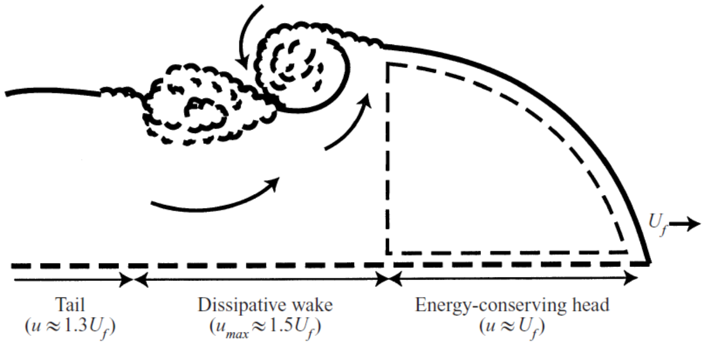

FIGURE 10. Schematic representation of the two-dimensional flow structure within a symmetric intrusion, in which u represents the fluid velocity within the current. Only the upper half of the intrusion is shown; the intrusion is assumed to be symmetric about the thick horizontal dashed line.

Figure 2.1: Schematic of a density current taken from Lowe et al. (2002) illustrating where the fastest winds were found in their study, as well as the dissipative wake and internal flow.

These wind characteristics within the density current have been shown to apply to cold pools. These higher wind velocities have been observed to be strongest during the mature stage of the cold pool life cycle, rapidly weakening during the dissipating stage of the cold pool life cycle (Engerer et al. 2008). Depending on the vertical wind profile, cold pools typically have gustier wind associated with them due to the transport of air from the midlevels down to the surface through convective downdrafts (Engerer et al. 2008). The strongest potential temperature perturbations are located near the surface within the first 5 km behind the leading edge of the cold pool, while the strongest winds are located directly behind this temperature perturbation, in the cold pool body (Grant and van den Heever 2016). Cold pools have also been observed to have a higher water vapor mixing ratio compared to the ambient environment (Karan 2014).

Higher values of moisture are often found collocated with areas of convergence, suggesting that moisture convergence may be important for MAHTE formation. Faster winds in the body of the density current result in convergence at its leading edge.

Moisture flux convergence (MFC) is the convergence of moisture in a location associated with the convergence of winds following the conservation of mass equations, given by

$$\mathrm{MFC} = -u\frac{\partial q}{\partial x} - v\frac{\partial q}{\partial y} - q\left(\frac{\partial u}{\partial x} + \frac{\partial v}{\partial y}\right),$$

where q is the specific humidity, and u and v are the horizontal wind components (Bancos and Schultz 2004). The importance of each term depends on the scale at which this convergence is occurring. On the scale of synoptic fronts, convergence and advection terms are comparable in magnitude, while for mesoscale boundaries such as sea breezes or thunderstorm outflow boundaries, horizontal mass convergence is an order of magnitude larger than the advection terms (Bancos and Schultz 2004). MFC leads to an increase in the depth of moisture in the area of surface convergence. Increases in vertical mixing in the boundary layer will thus be less impactful on removing moisture from this deeper area of moisture, which will result in a localized area with higher moisture content as the afternoon progresses (Markowski and Richardson 2008). This is one mechanism that could potentially explain why the cold side of thermal boundaries can have higher θ_e by the early afternoon hours, given MFC and equal insolation across the boundary.

In addition to causing MFC along the leading edge of the cold pool, changes to wind speed, temperature, and moisture content in the cold pool can also have impacts on surface fluxes. One way to undergo irreversible changes to entropy and thus θ_e is through surface fluxes of energy and moisture. Energy is primarily transported from the surface to the atmosphere through two mechanisms, sensible heat fluxes and latent heat fluxes. One way to see how the changes in meteorological conditions commonly observed in cold pools will affect the surface heat fluxes is through the bulk aerodynamic formulas adapted from Yokoi et al. (2014). Sensible heat flux is given by

$$\mathrm{SHF} = \rho c_p C U(\theta_{sfc} - \theta_{air}),$$

and the latent heat flux is given by

$$\mathrm{LHF} = \rho L_v C U(q_{sfc} - q_{air}),$$

where ρ is the surface air density, c_p is the specific heat of moist air at constant pressure, L_v is the latent heat of vaporization of water, C is the bulk transfer coefficient of heat and moisture, U is the surface wind speed, θ is the potential temperature of the surface or air, and q is the specific humidity of the surface or air. From these equations, it is apparent that the surface heat flux will increase with increasing temperature difference between the air and the surface, and with increasing wind speeds. Similarly, latent heat flux will increase with increasing humidity difference between the surface and air, and with increasing wind speeds. The latent heat flux can be related to the moisture flux from the surface, F_{water}, through

$$F_{water} = \frac{\mathrm{LHF}}{L_v}.$$

Examining the factors which control the exchange of moisture with the surface and the atmosphere can provide insight into the potential mechanisms for MAHTE formation. Decreases in moisture content combined with stronger winds in thunderstorm outflow could act to increase the surface moisture flux, resulting in a localized increase in moisture content. Several cold pool studies (Young et al. 1994; Yokoi et al. 2014; Schlemmer and Hohenegger 2015; Skyllingstad and Szoeke 2015) have found that an increase of wind speed within cold pools was the primary cause of increases in observed surface latent heat fluxes, rather than due to the decreases of moisture typically observed within cold pools. It was demonstrated that moisture fluxes can be responsible for 30% of the moisture anomaly found in the cold pool head (Schlemmer and Hohenegger 2015).

Multiple studies of cold pools over tropical oceans have documented examples where rings of moisture are found at the leading edge of cold pools. Thompson (2001) found that these areas of increased moisture were associated with areas of higher θ_e and CAPE, similar to a MAHTE. Thompson (2001) attributed this increase in moisture to the evaporation of rain and advection of this initial evaporation-enhanced area of moisture to the leading edge of the cold pool with the first development of the thunderstorm downdraft. The increase in moisture at the leading edge of thunderstorm outflow can also be explained by changes to surface fluxes in cold pools. Longhans and Romps (2015) attributed the primary cause of these areas of increased moisture along thunderstorm outflow to latent heat fluxes from the surface. As cold pools expand laterally, the absolute instability which forms as a result of the temperature difference between the surface and the cold pool can generate turbulent kinetic energy, which will result in an intensification of both sensible and latent heat fluxes from the surface (Ross et al. 2004). These increases in surface latent heat fluxes can maintain any humidity anomaly found in the cold pool head as it spreads, which further acts to reduce vertical mixing impacts on moisture in the cold pool head (Ross et al. 2004). Other potential sources for the formation of these rings of higher moisture could include the evaporation of rain, and the advection of preexisting boundary layer moisture (Seifert and Heus 2013; Schlemmer and Hohenegger 2015).

Along with wind having an impact on surface moisture fluxes, perturbations to temperature and moisture can also have an impact on surface fluxes and resulting MAHTE formation. Temperature differences between tropical cold pools and the ocean surface can create a nearly 300% increase in surface sensible heat flux (Young et al. 1994). Sensible heat fluxes are also increased due to increasing wind speed, however this increase in sensible heat flux is primarily caused by increased temperature differences between the surface and the cold pool air (Yokoi et al. 2014). Increasing the surface roughness length in simulated cold pools also increases the surface heat fluxes (Gentine et al. 2016). This is due to increasing the turbulence in the cold pool near the surface, which intensifies the surface and sensible latent heat fluxes (Ross et al. 2004).

Examining how cold pools evolve and dissipate can provide insight into another potential cause for MAHTE formation. Dissipation of simulated cold pools through surface fluxes leads to a warming and moistening in the body of the cold pool (Seifert and Heus 2013). One of the main causes of cold pool dissipation and recovery is the entrainment of air into the cold pool through Kelvin-Helmholtz waves which form along the top of cold pools (Grant and van den Heever 2015). The impact of surface fluxes on the static stability of the cold pool and the resulting entrainment plays a more significant role on the evolution of the cold pool than just the impact of surface heat fluxes alone (Grant and van den Heever 2015).

This goal of this study is to address the characteristics of MAHTEs, and the processes responsible for their formation and evolution. Surface characteristics of the MAHTE will be determined using surface observations, while processes responsible for their formation will be examined through high resolution numerical simulations as these processes in MAHTE formation and evolution cannot be determined from surface observations alone. It is hypothesized that:

1. A primary mechanism for MAHTE formation is differential vertical advection across the boundary. As vertical advection is suppressed in the cool air compared to the ambient environment, higher moisture within the colder air mass will remain in place as solar insolation raises the θ_e through time.
2. As θ_e is a conserved variable, initially higher θ_e air is lifted above and entrained into the cold pool as it dissipates. As differential vertical advection occurs and with solar insolation, the θ_e in the cold pool increases to values above those observed in the ambient environment.
3. Increased surface fluxes within the colder air mass due to increased temperature perturbations and increased winds will result in maintenance or even an increase in moisture within the MAHTE.

Chapter 3

Observational Component

3.1 Methodology

This analysis focuses on a MAHTE that occurred along the cool side of a slowly moving, east-west oriented synoptic cold front in northwestern Kansas on 20 June 2016. Four transects of the MATHE were made between 1900 and 2300 UTC, from roughly 20 km south of the boundary in the warm air mass, to roughly 40 km north of the boundary in the cool air mass. Surface observations of temperature, relative humidity, pressure, and wind direction and speed were collected using an Integrated Mesonet and Tracker (IMeT). Information on IMeT sensor models and their accuracy can be found in Table 3.1. The surface data were transformed to a boundary relative frame of reference following the methodology of Riganti and Houston (2016) for analysis, where positions of the boundary were taken as the southern edge of the 20 dBZ reflectivity fine line observed by the Goodland, Kansas, Weather Surveillance Radar 1988 Doppler (WSR-88D). Due to the less defined nature of the boundary at the initial times of the study, the location of the boundary is more approximate during the initial transects compared to the later transects.

Table 3.1: Information on sensors used on the IMeT

Component	**Model**	**Output**	**Accuracy**
RH and slow-temperature	Vaisala HMP155A-L-PT	Temp: -80 to +60 °C RH: 0 to 100%	Temp: ±(0.226 - 0.0028 × temperature)°C RH: ±(1.0 + 0.008 × reading) % RH Response time: 20s
Fast temperature	Campbell Scientific 109SS-L Thermistor	-40° to +70 °C	± 0.1 C Response time: 7.5 s (3 m s^{-1})
Pressure	Vaisala PTB210	500-1100 hPa	± 0.25 hPa
Wind	RM Young 05103-L-PT	WS: 0 to 100 m s^{-1} WD: 0 to 360 °	WS: ± 1% WD: ± 3

Rapid Refresh (RAP) model point soundings were obtained to examine how the MAHTE would impact other forecast parameters, such as CAPE. CAPE for these modified soundings was calculated using SHARPpy (Bloomberg et al. 2017). For these modifications, surface observations of temperature and dewpoint temperature in the ambient warm environment 10 km south of the cold front and within the MAHTE where the maximum value of θ_e was observed were used as the modified sounding surface observations. Sounding modifications were done to examine how surface based convective available potential energy (SBCAPE) changes across the boundary. Examining how the MAHTE modifies the local environment can provide insight into how a local storm would evolve if it were to interact with the MAHTE, allowing for some inference and comparison with past observed cases of MAHTEs.

One important issue with MAHTEs noted previously is that their small areal extent makes observing them with the current National Weather Service surface observation network difficult. During the late afternoon, this MAHTE passed over the Colby, Kansas automated surface observation station (ASOS) (Figure 3.1). To compare the collected observations of a MAHTE to how an ASOS station would resolve a MAHTE, 20 minute data from the Colby, Kansas ASOS was obtained, and θ_e was calculated for each available time.

3.2 Results

3.2.1 Synoptic Overview

At 1800 UTC on 20 June 2016, there was an east-northeast to west-southwest oriented cold front over extreme northwestern Kansas into southcentral Nebraska moving slowly to the south (Figure 3.1). The front was most apparent in the surface wind field, as the temperature gradient across the boundary was rather diffuse. Temperatures of 25-30 °C were reported in Nebraska, and 31-34 °C in Kansas. Winds north of the boundary were from the northeast, with southwesterly winds to the south of the boundary. Dewpoint temperatures were relatively similar across the cold front, ranging from 15 °C in Nebraska, and 20 °C to the south of the cold front. Midlevels were characterized by a trough at 500 hPa positioned over the southcentral United States. By 0000 UTC 21 June 2016, the surface cold front had progressed slightly farther to the south, with temperatures across central Kansas reaching the as high as 36 °C, and with 26-27 °C across Nebraska (not shown). Based on the synoptic-scale observations, dewpoint temperatures remained at 15-17 °C across the region. Throughout the day, winds at 850 hPa were out of the south across the entire region. By 2000 UTC 20 June 2016, storms had formed approximately 150 km to the north of the cold front, and progressed towards the east-southeast.

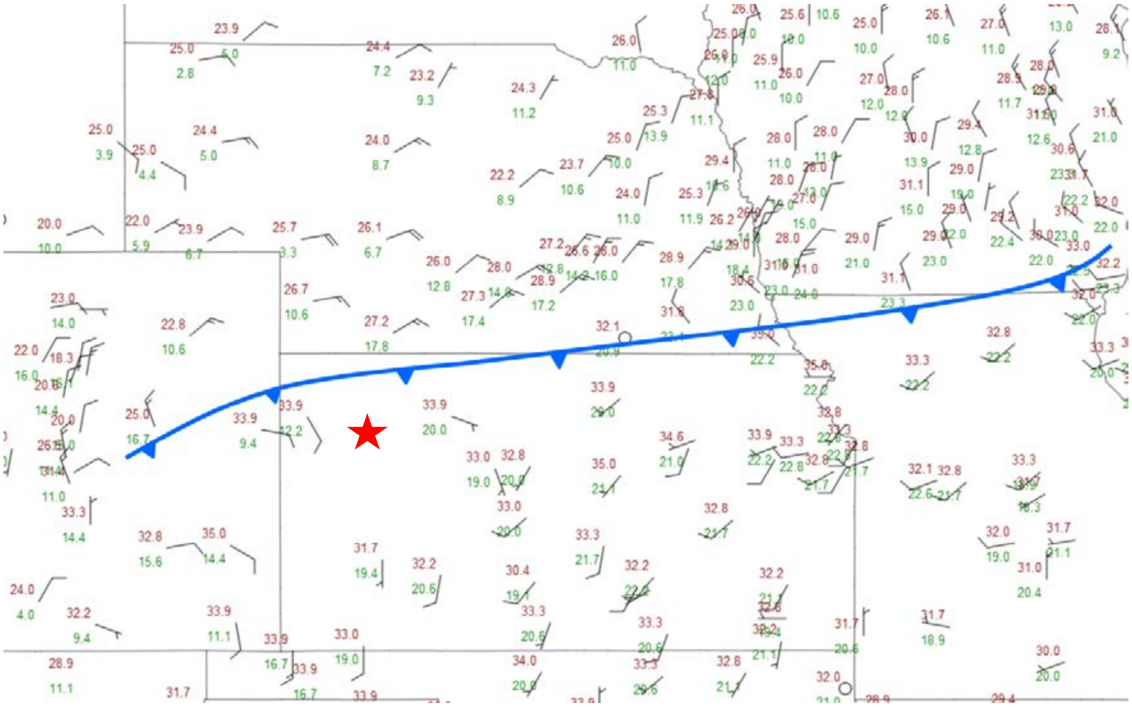

Figure 3.1: Synoptic surface observations at 1800 UTC when surface transects first began. The annotated location of the cold front is indicated in blue, with the location of the Colby, Kansas, ASOS station (observations unreported on this map at this time) indicated by the red star.

3.2.2 Characteristics of the MAHTE

The location and evolution of the synoptic cold front is indicated by the reflectivity fine line in Figure 3.2. Transects of the MAHTE were collected roughly perpendicular to the cold front, as indicated by the blue lines in Figure 3.2. The goal of these transects was to capture the characteristics of the warm environment, the MAHTE, and the location north of the cold front where θ_e returned to values observed in the warm air mass.

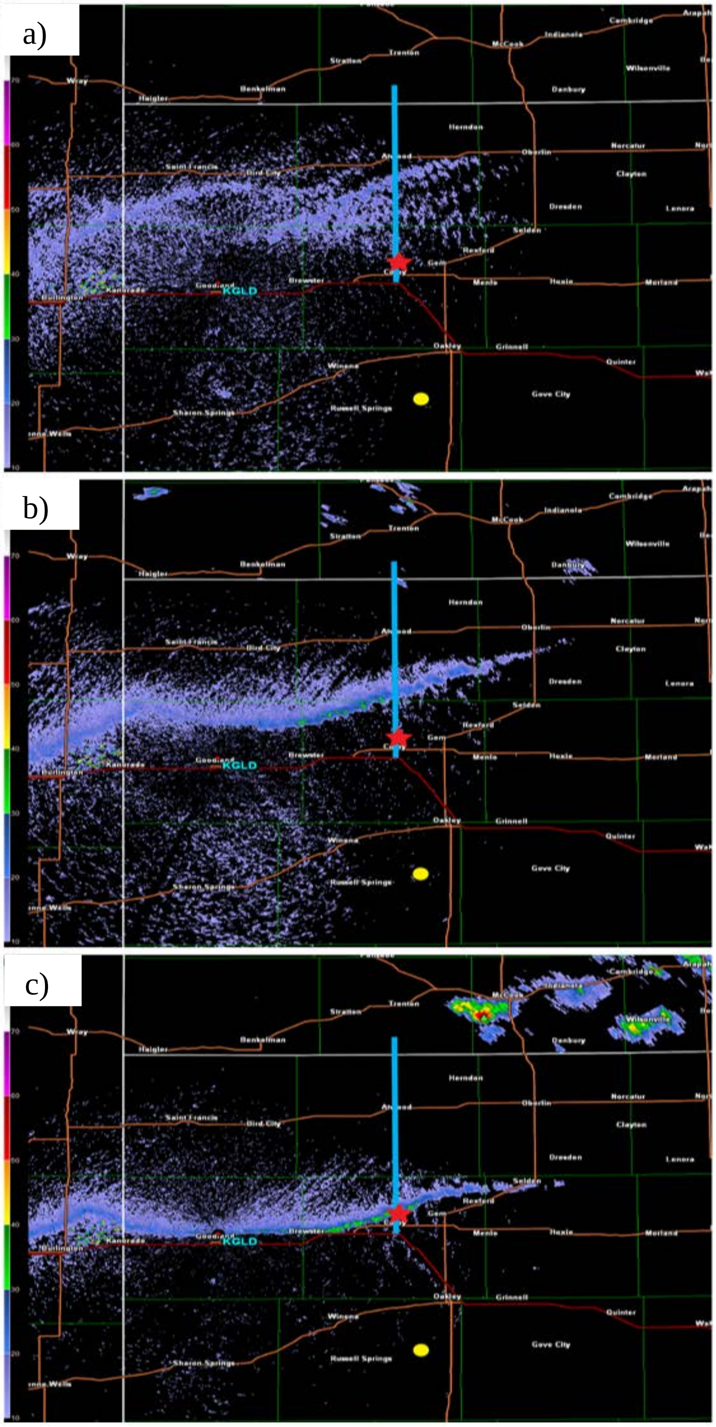

Figure 3.2: Goodland Kansas WSR-88D observations of the cold front mesoscale evolution not adequately captured by the ASOS observation network at a) 1859 UTC, b) 2101 UTC, and c) 2259 UTC. Also shown are the approximate locations of the surface transects (blue line), the location of the Colby, Kansas ASOS station (red star), and the location of the modified RAP soundings (yellow dot).

The maximum θ_e during each transect was observed to be approximately 2 – 6 km behind the leading edge of the boundary (Figure 3.3). The highest θ_e (372.9 K) was observed during the first transect at 1942 UTC, and steadily decreased during subsequent transects (Figure 3.3). The maximum θ_e was observed near the maximum dewpoint temperature in most transects. Similar to θ_e, the maximum dewpoint temperature (23.4 °C) was observed during the first transect. The maximum θ_e was 12.2 K higher than the θ_e observed at the boundary, and 19.8 K higher than that observed in the warm sector. This was due to an increase in dewpoint temperature of 5.8 °C (Figure 3.4), despite the corresponding drop in temperature of 1 – 2 °C (Figure 3.5). In general, transects revealed that the MAHTE had θ_e values that were 13 – 20 K higher than the ambient environment (Figure 3.3), and a dewpoint temperature that was 6 to 8 °C higher than the ambient environment (Figure 3.4). Within the MAHTE, θ_e and dewpoint temperature decreased as the afternoon progressed, though temperature within the MAHTE remained nearly constant despite insolation. On the warm side of the boundary, θ_e remained nearly constant throughout the afternoon.

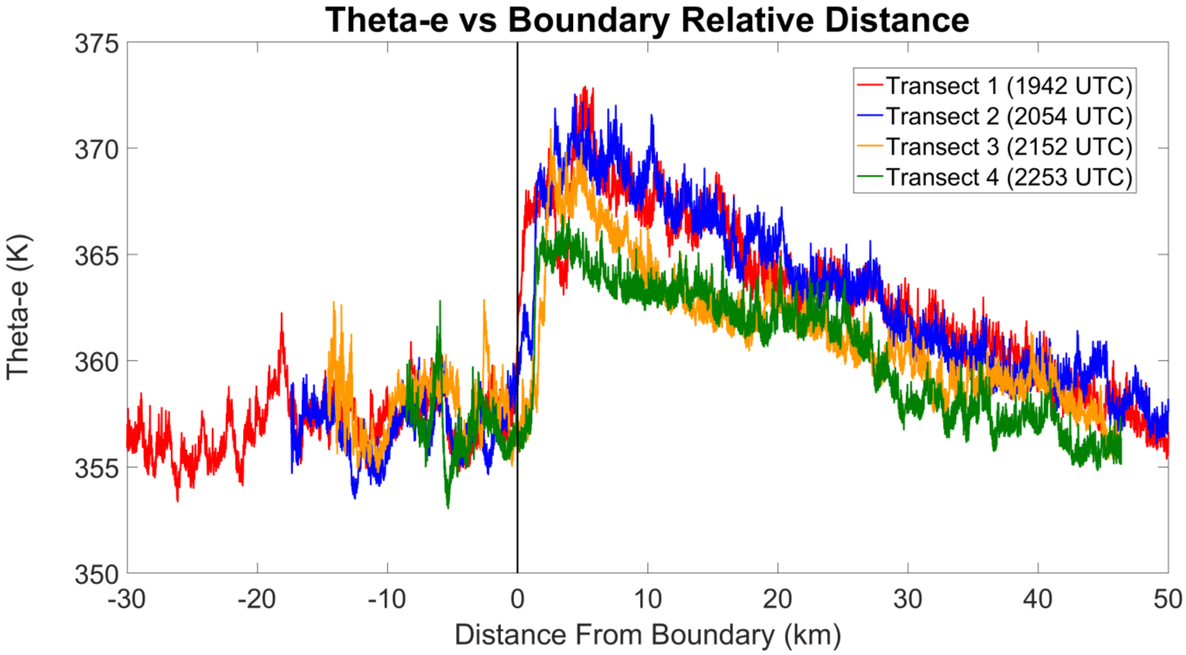

Figure 3.3: Observed θ_e during each transect. Observations are transformed into a boundary-relative frame of reference, where positive distances represent the cool side of the boundary, and negative distances represent the warm side of the boundary. UTC times indicate when the boundary was crossed.

Throughout the observation period, winds to the south of the boundary were out of the south, while winds to the north of the boundary were out of the northeast (Figure 3.6). Winds to the south of the boundary remained constant in magnitude and direction despite the likely deeper vertical mixing due to winds of similar magnitude existing throughout the lower levels of the atmosphere as indicated by nearby RAP soundings, which will be discussed in further detail in the next section.

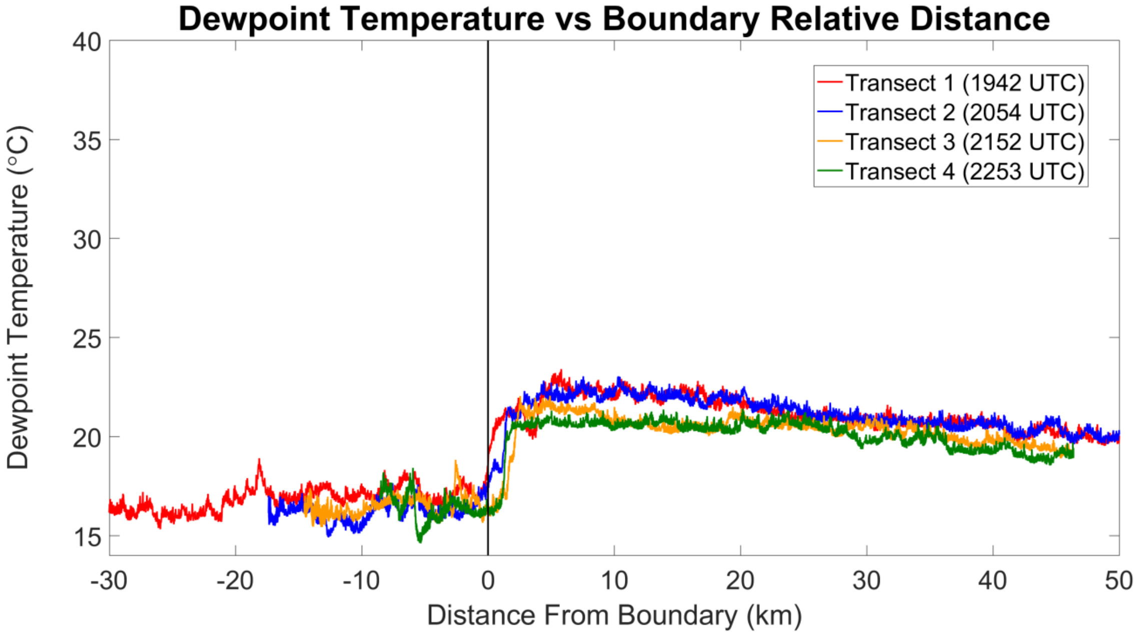

Figure 3.4: Observed dewpoint temperature during each boundary transect in a boundary relative frame of reference as in Figure 3.3.

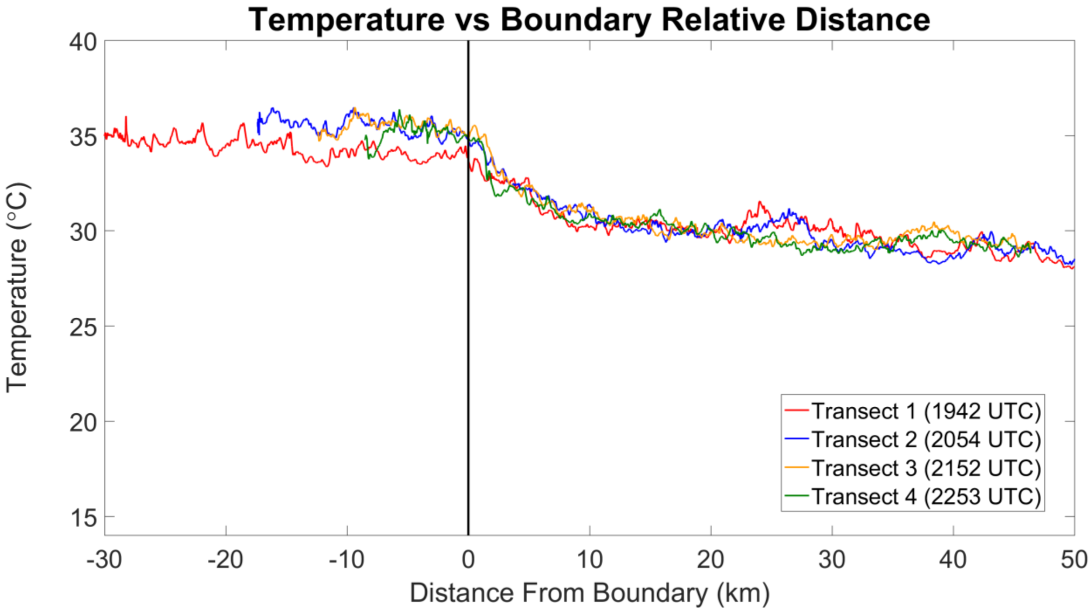

Figure 3.5: Observed temperature during each boundary transect in a boundary relative frame of reference as in Figure 3.3.

The width of a MAHTE is defined here as the distance from the boundary to the point on the cool side where θ_e first drops back to the θ_e observed at the boundary. Based on this definition, the 20 June 2016 MAHTE had an approximate width of 30 – 45 km (Figure 3.3), which is wider than what was anticipated based on the theoretical model of MAHTE widths. Due to the sensitivity of the MAHTE width to the position of the boundary, calculations of the MAHTE width were also confirmed through manual analysis. The smaller theoretical size compared to our results could be due to limited observations of past MAHTE. Even with transects of MAHTE during the VORTEX-95 field campaign, researchers were not explicitly looking for the width of the θ_e maximum on the cold side of the boundary, so the exact width of the 02 June 1995 MAHTE is not known. Although Gronemeijer et al. (2011) did not examine the exact point at which θ_e or dewpoint temperature reached magnitudes comparative with the warm sector, they found that SBCAPE was higher in the MAHTE compared to the non-zero SBCAPE in the warm environment, and reached zero approximately 60 km north of the warm front. This indicates that their MAHTE width would be less than 60 km.

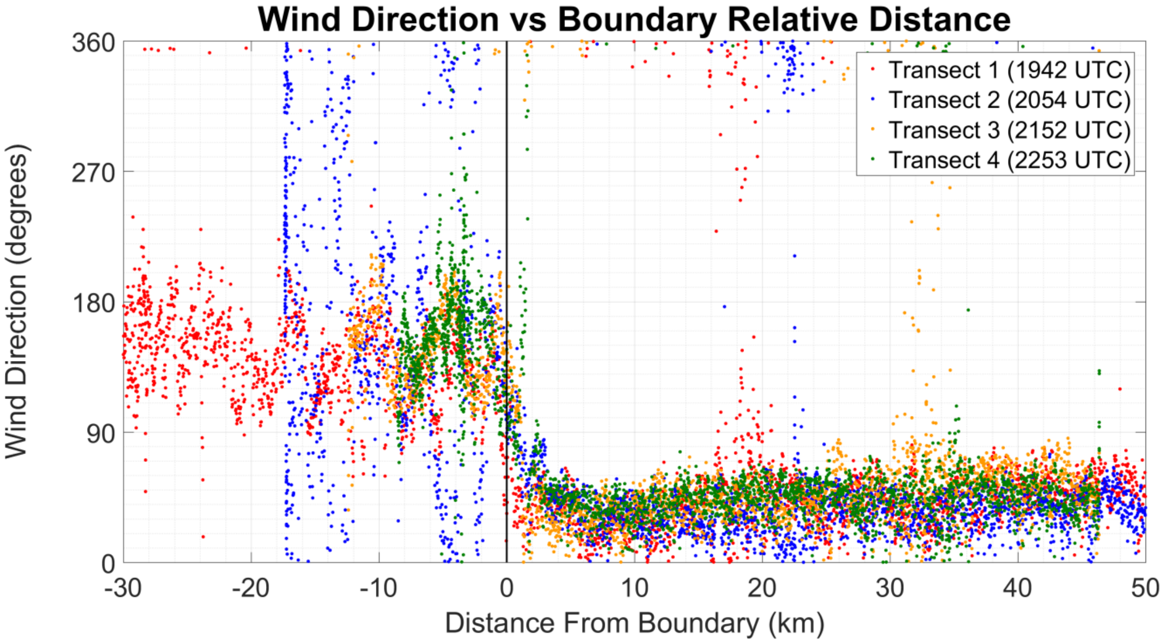

Figure 3.6: Observed wind direction during each boundary transect in a boundary relative frame of reference as in Figure 3.3.

3.2.3 Sounding Modifications

Observations collected by the IMeT were used to modify RAP soundings to examine the possible impact of the MAHTE on SBCAPE. Vertical profiles from RAP analysis grids at 2000 and 2300 UTC were modified with data collected at the approximate time of the MAHTE transects. Initial RAP profiles representative of the air mass south of the boundary were extracted at a point approximately 25 km south of Colby, Kansas, as indicated in Figure 3.2. IMeT observations of temperature and dewpoint temperature from the location of maximum θ_e at each transect were used for the near-surface conditions for the MAHTE sounding. Inferred low-level profiles of temperature were developed by assuming that IMeT near-surface observations of temperature were well-mixed through a 100 hPa layer. Profiles of moisture within the

MAHTE were developed by setting the surface dewpoint temperature to that observed by the IMeT at the location of maximum θ_e; moisture content was not assumed to be well mixed as it is difficult to know what the exact moisture profile would look like through the convective boundary layer. Representative warm environment soundings were similarly modified by IMeT observations collected approximately 10 km south of the boundary.

Figure 3.7 shows how SBCAPE changed by modifying the soundings with MAHTE data. At 2000 UTC, RAP soundings modified with the warm sector observations showed that SBCAPE was 2159 J kg^{-1}, while the MAHTE modified sounding had an SBCAPE of 6843 J kg^{-1}. This difference in SBCAPE is mainly due to the higher moisture in the MAHTE. Throughout the observation period, SBCAPE for the modified warm sector soundings remained between approximately 2200 to 2600 J kg^{-1}, while SBCAPE for the modified MAHTE soundings decreased steadily in magnitude from approximately 6800 to 5000 J kg^{-1}. This shows that the MAHTE could have had 2000 to 3000 J kg^{-1} higher SBCAPE than the warm sector. These changes in SBCAPE across the boundary were much greater than those discussed by Rasmussen et al. (2000) or Gilmore and Wicker (2002), however their dataset recorded a difference in θ_e of approximately 10 K between the warm sector and the MAHTE, while our observations were characterized by differences of 13 – 20 K. Combined with the favorability of shear profiles along thermal boundaries (Maddox et al. 1980), these increases in SBCAPE could impact the evolution of storms encountering a MAHTE through increased updraft strength.

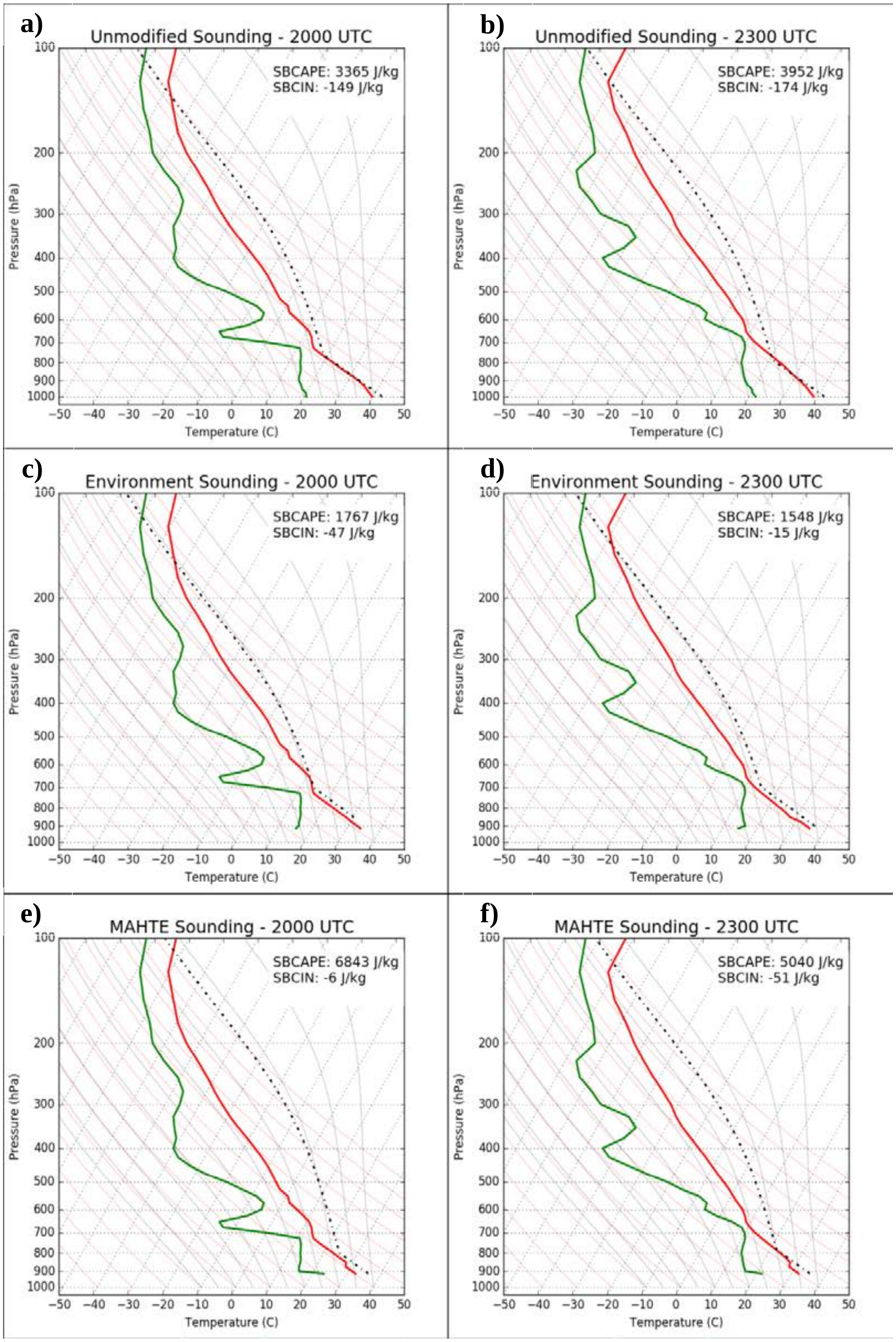

Figure 3.7: a) and b) unmodified RAP soundings, c) and d) RAP soundings modified with surface observations in the warm environment, and e) and f) RAP soundings modified with surface observations in the MAHTE.

3.2.4 ASOS station comparison

To compare how the National Weather Service observation network would resolve a MAHTE, data from the Colby, Kansas ASOS (hereafter KCBK; Figure 3.1) over the period of our analysis was examined. Prior to the cold front passing KCBK, θ_e was observed to be 360 – 364 K before 1700 UTC, and then dropped to 358 – 361 K in the afternoon (Figure 3.8). θ_e in the warm environment as observed by KCBK was approximately 1 – 3 K higher than what was observed during the MAHTE transects, likely due differences in instrument resolution. The MATHE passed KCBK at approximately 2300 UTC on 20 June 2016 with a corresponding drop in temperature while θ_e rose approximately 10 K to a maximum value of 367 K. This was of equal magnitude to the peak value of θ_e in the MAHTE observed in the final surface transect near this time. One hour after the passage of the MAHTE, θ_e dropped to values below those observed in the warm air mass during the afternoon, likely due to the continued southward propagation of the MAHTE. This illustrates that MAHTEs can be resolved when they interact with an observation station; however, due to the limited areal coverage of our current observation network, it is still difficult to adequately resolve the formation of every MAHTE.

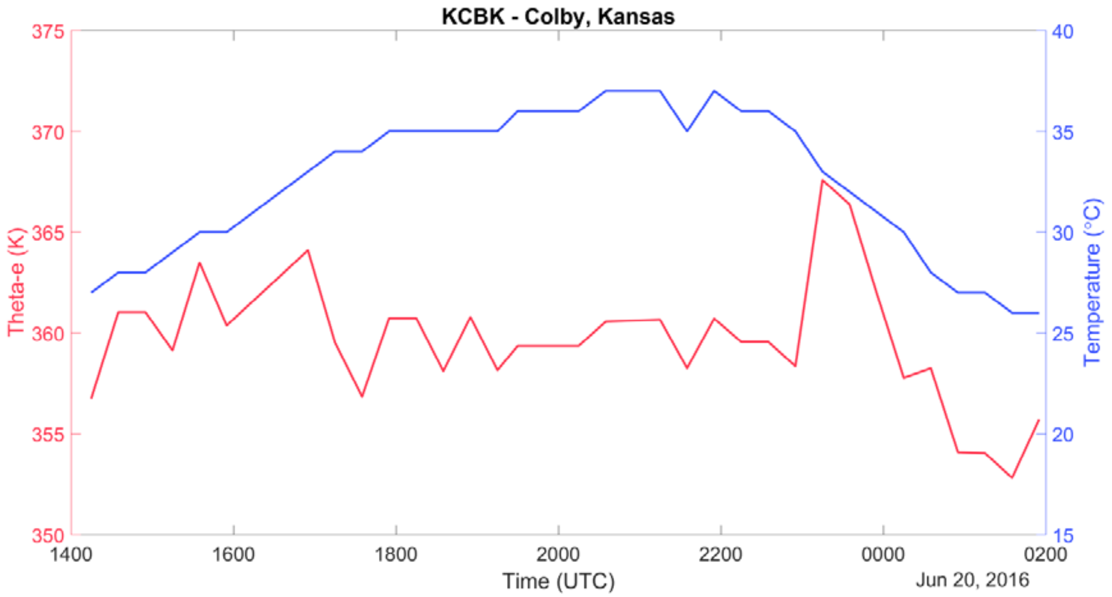

Figure 3.8: Surface observations of θ_e (K, in red) and temperature (°C, in blue) from the Colby, Kansas ASOS station (KCBK), from 1400 UTC, 20 June 2016 to 0200 UTC, 21 June 2016. The MAHTE passed over KCBK at approximately 2300 UTC.

Chapter 4

Modeling component

4.1 Methodology

The Advanced Research Weather Research and Forecasting model version 3.8 (WRF-ARW; Shamarock et al. 2008) was utilized for the modeling component of this study. WRF was initialized using analysis fields from the 4-km North American Mesoscale (NAM) forecast system. The outer domain of this study was 950 by 750 km and had a grid spacing of 1 km, with an inner domain of dimensions 150 by 150 km nested down to 333 m grid spacing (Figure 4.1). Ninety vertical levels were selected, preferentially stacked within the boundary layer with approximately 38 levels below 2 km, and the lowest level at 25 m AGL. The high resolution was chosen to ensure that all processes occurring within the small MAHTE area would be accurately resolved. This inner domain was centered near Atwood, Kansas, as this was the approximate location of the observations collected across the MAHTE in the afternoon for this event. The model was initialized at 1400 UTC 20 June 2016, 5 hours before the MAHTE formed, to allow adequate spin up time, and to allow for analysis of the conditions leading up to MAHTE formation. The model was run without nudging until 0200 UTC 21 June 2016.

Simulations used the Rapid Radiative Transfer Model (RRTM) radiation longwave radiation parameterization (Mlawer et al. 1997) with the Dudhia shortwave radiation parameterization (Dudhia, 1989). The RRTM longwave radiation scheme was selected because of its accuracy in accordance with line-by-line calculations of radiative transfer (Mlawer et al. 1997). The Morrison microphysics parameterization (Morrison et al. 2009) was selected for the microphysical scheme. This is a two-moment microphysics scheme that parameterizes 5 different water phases and is ideally suited for accurate representation of deep convective processes. Although deep convection is not simulated in this work, storm-generated MAHTEs will be the focus of future work and Morrison microphysics are therefore included for consistency with this subsequent research. The Mellor–Yamada–Nakanishi–Niino (MYNN) planetary boundary layer (PBL) and surface physics schemes were selected in accordance with a study conducted by Coniglio et al. (2013) which found that this scheme produced a more accurate representation of the convective boundary layer compared to other WRF PBL schemes. It was also found that in addition to more accurate prediction of PBL height, afternoon temperature and moisture were nearly unbiased (Coniglio et al. 2013). Finally, the unified Noah land-surface model (Tewari et al. 2004) was selected as the land-surface scheme in accordance with past mesoscale studies (Coniglio et al. 2013; Burghardt et al. 2014). The unified Noah land-surface model has four soil layers, and calculates soil moisture and temperature, as well as surface energy fluxes. This land-surface model has one vegetation layer, and only assigns one vegetation type per grid cell when making temperature and flux calculations (Liang et al. 2012). Other more complex surface models, such as the Community Land Model (CLM4), utilize 10 soil layers, with differing drainage calculations. The CLM assigns a grid cell with up to 10 differing vegetation types, and calculates temperature and surface energy fluxes for eight sub-grids (Oklaebo et al. 2016). Due to the high resolution of our simulations, it is assumed that the Noah land-surface will be sufficient for representing surface energy fluxes in this study. Future work will include comparing different land-surface models to address how surface fluxes might change within a MAHTE.

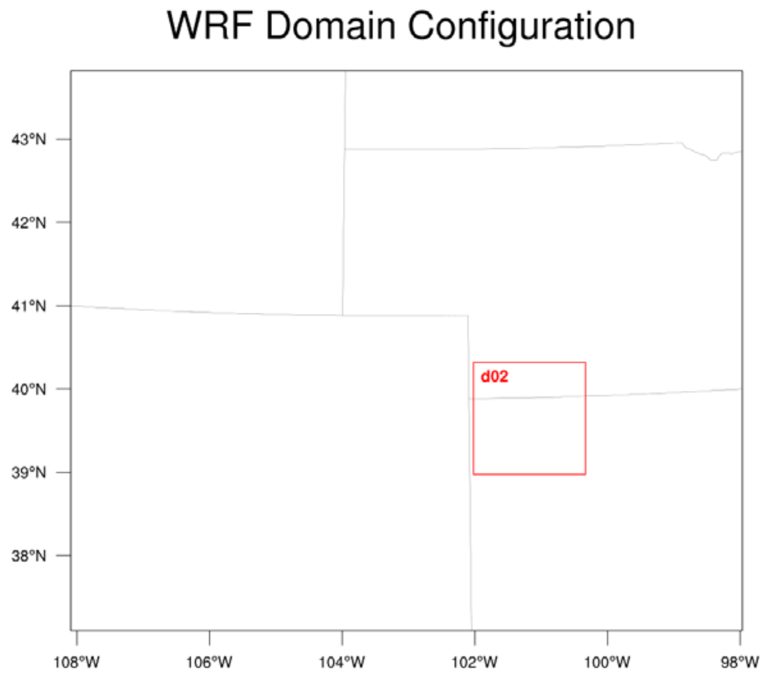

Figure 4.1: WRF domain configuration used for simulations. Domain 2 was used for all analyses.

To examine the time evolution of surface variables during MAHTE formation, averages were calculated over two 15 by 15 km areas: 1) one area was located where the values of θ_e initially rose the most rapidly, and 2) one area was to the south of the boundary. Averages taken in areas representative of MAHTE formation and the warm environment allow for an examination and comparison of variables which can change θ_e to determine what is responsible for MAHTE formation. These areas are illustrated as the polygons in Figure 4.2; they remained in those locations throughout the analysis.

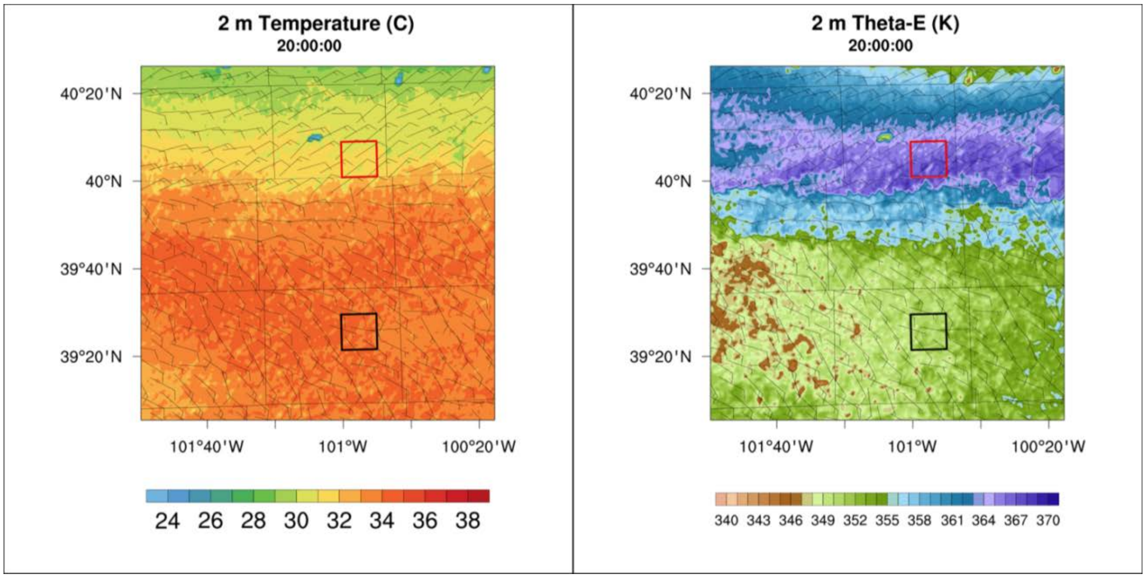

Figure 4.2: 15 by 15 km areas used for variable averages overlaid on temperature and θ_e at 2000 UTC. Red box indicates the area representative of the MAHTE, and black box the area representative of the warm environment.

4.2 Results

4.2.1 Comparison of the simulation to observations

The simulation was initialized with the cold front at 40˚ N. Once the MAHTE had formed by 2200 UTC, there was a change in θ_e of approximately 15 K across the front, similar to the difference in θ_e across the front in observations discussed in the previous section. The maximum θ_e was approximately 372 K directly on the cold side of the cold front, similar to what was observed in the surface transects. Dewpoint temperatures in the simulations reach a maximum value of approximately 22 °C within the MAHTE. This is 1 °C lower than the maximum in observed dewpoint temperatures within the MAHTE; however the difference in dewpoint across the cold front is approximately 6 °C, similar to observations. Due to the accurate representation of surface variables, we will assume that the processes within the MAHTE that contribute to MAHTE formation and evolution in the simulation are characteristic of what would be observed in the atmosphere.

4.4.2 Overview of simulated MAHTE formation and evolution

At 1400 UTC, when the model was first initialized, the simulated cold front, manifest principally in the wind field, was located near latitude 40˚ N (Figure 4.3a). Simulated 2-m θ_e was highest at this time to the south of the front (Figure 4.4a), while there was a diffuse southwest to northeast gradient in dewpoint temperature across the domain (Figure 4.5a). By 1600 UTC, temperatures increased more rapidly to the south of the front than to the north of the front (Figure 4.3b). The gradient in θ_e across a 10 km transect along the longitude of our surface transects was only 0.21 K km^{-1}, and was now directed north to south, due to the beginning of the reduction in dewpoint temperature to the south of the front (Figure 4.4b, 4.5b). Cross sections of θ_e show that θ_e was relatively uniform across the surface, with an area of lower θ_e aloft over the southern portion of the domain (Figure 4.6b). The transition to a convective boundary layer by 1800 UTC is associated with a decrease in θ_e south of the cold front (Figure 4.6c). From 1400 UTC to 1800 UTC, θ_e south of the cold front decreased by as much as 8 – 12 K, while θ_e steadily rose to be approximately 10 K higher north of the front (Figure 4.4c). This reduction of θ_e in the warm sector was due to a reduction in low-level moisture; average dewpoint temperatures across the southern subdomain decreased approximately 5 °C between 1600 and 1800 UTC (Figure 4.5a). Area averaged dewpoint temperatures to the north of the front remained largely unchanged (Figure 4.7). By 1800 UTC, average temperatures were higher across the entire domain but more significant warming had occurred across the warm sector compared to the cold sector (Figure 4.7).

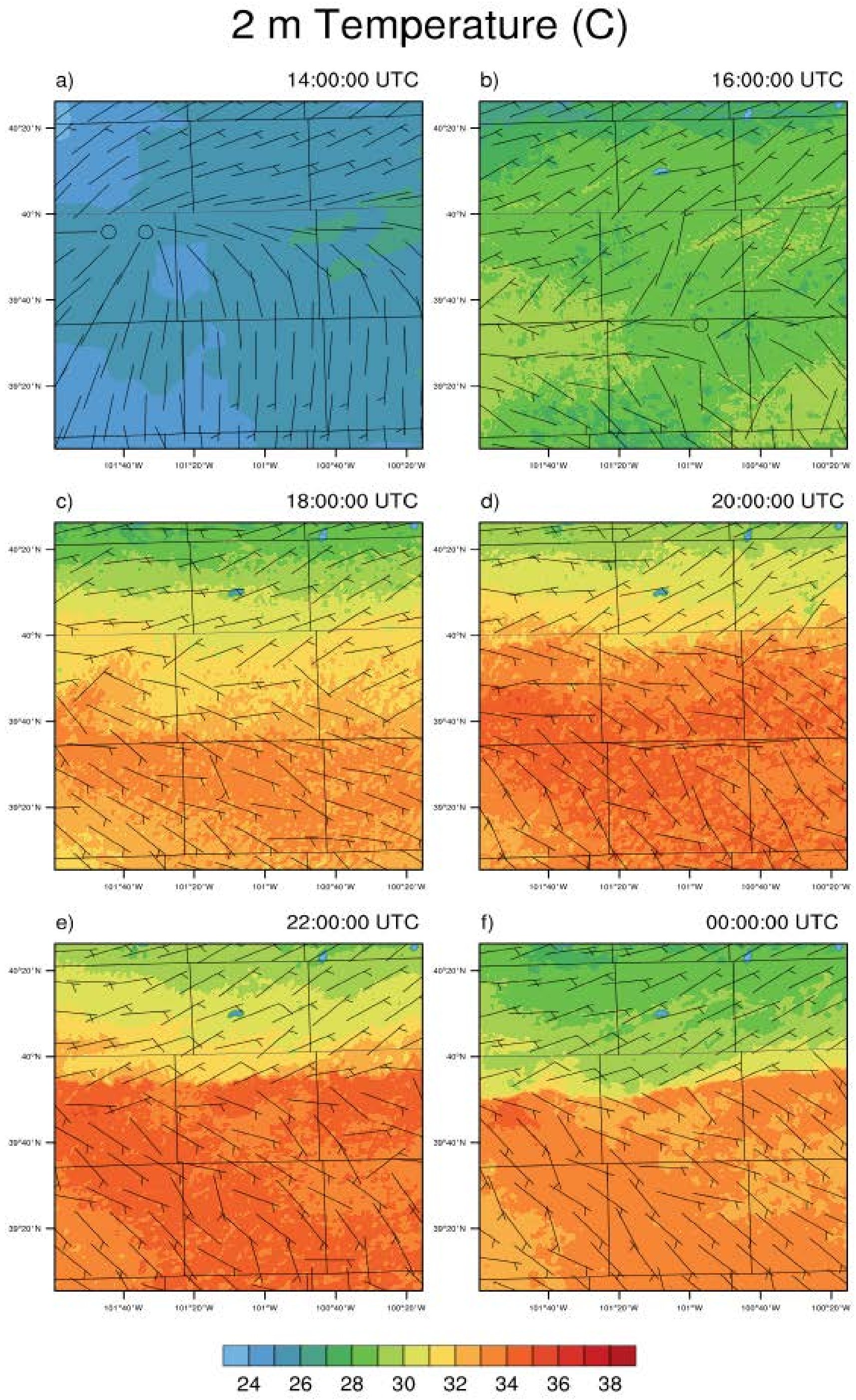

Figure 4.3: Simulated 2-m temperature (°C) and 10-m winds (m s^{-1}) at a) initialization of the model, b) and c) prior to the development of the MAHTE, d) during MAHTE formation, e) at peak intensity of the MAHTE, and f) the beginning of the dissipation of the MAHTE.

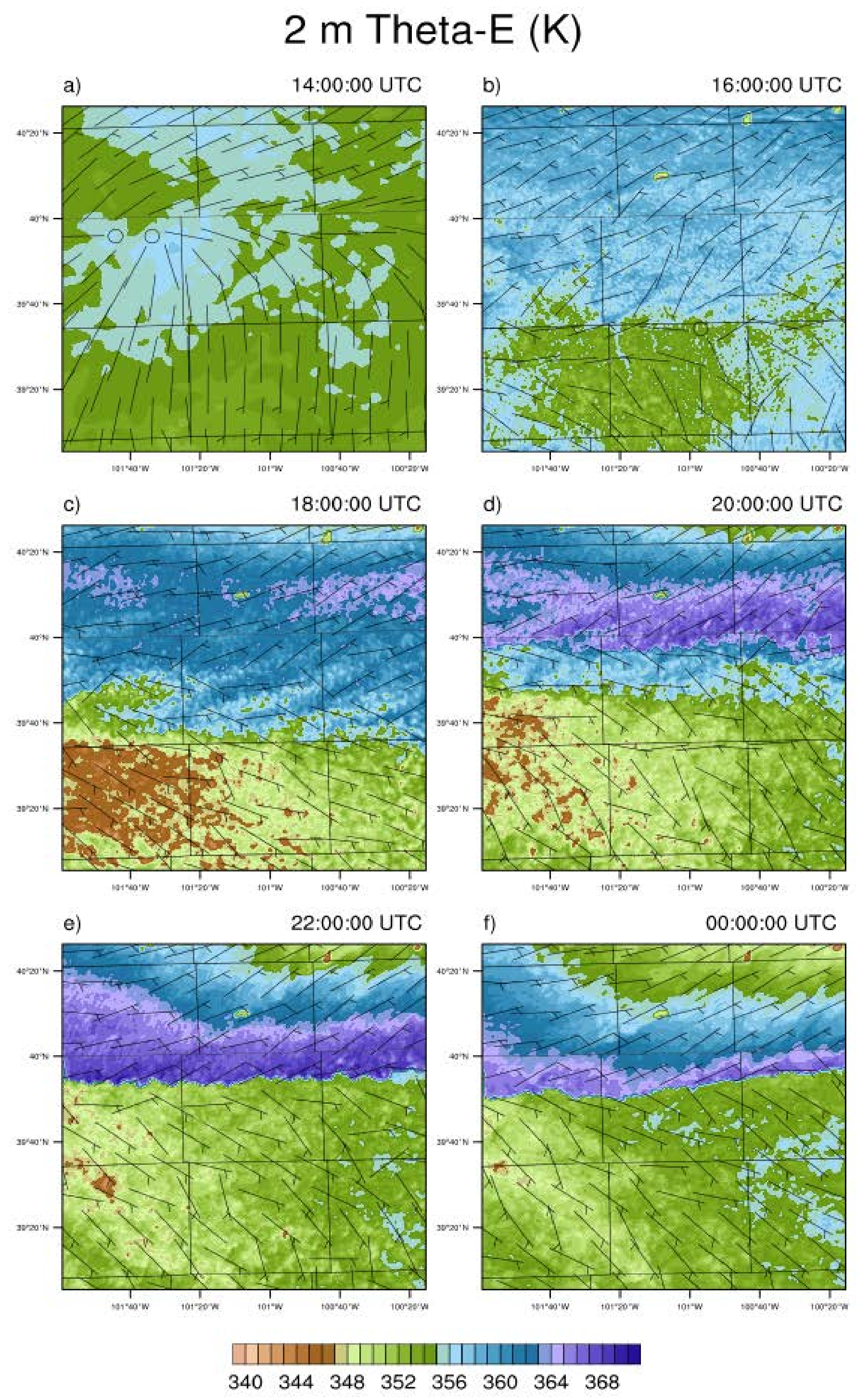

Figure 4.4: As in Figure 4.3 except simulated 2-m θ_e (K) and 10-m winds (m s^{-1}).

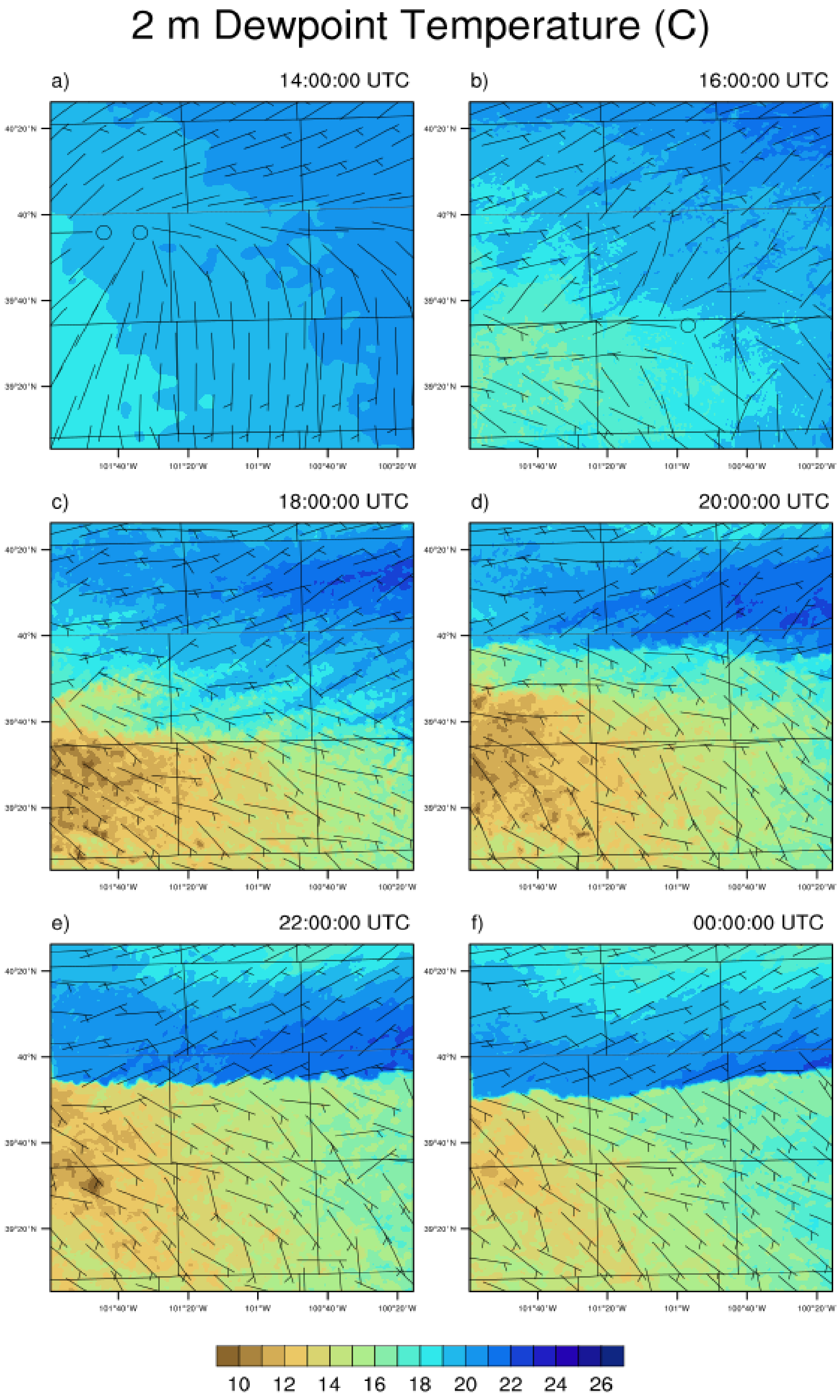

Figure 4.5: As in Figure 4.3 except simulated 2-m dewpoint temperature (°C) and 10-m winds (m s^{-1}).

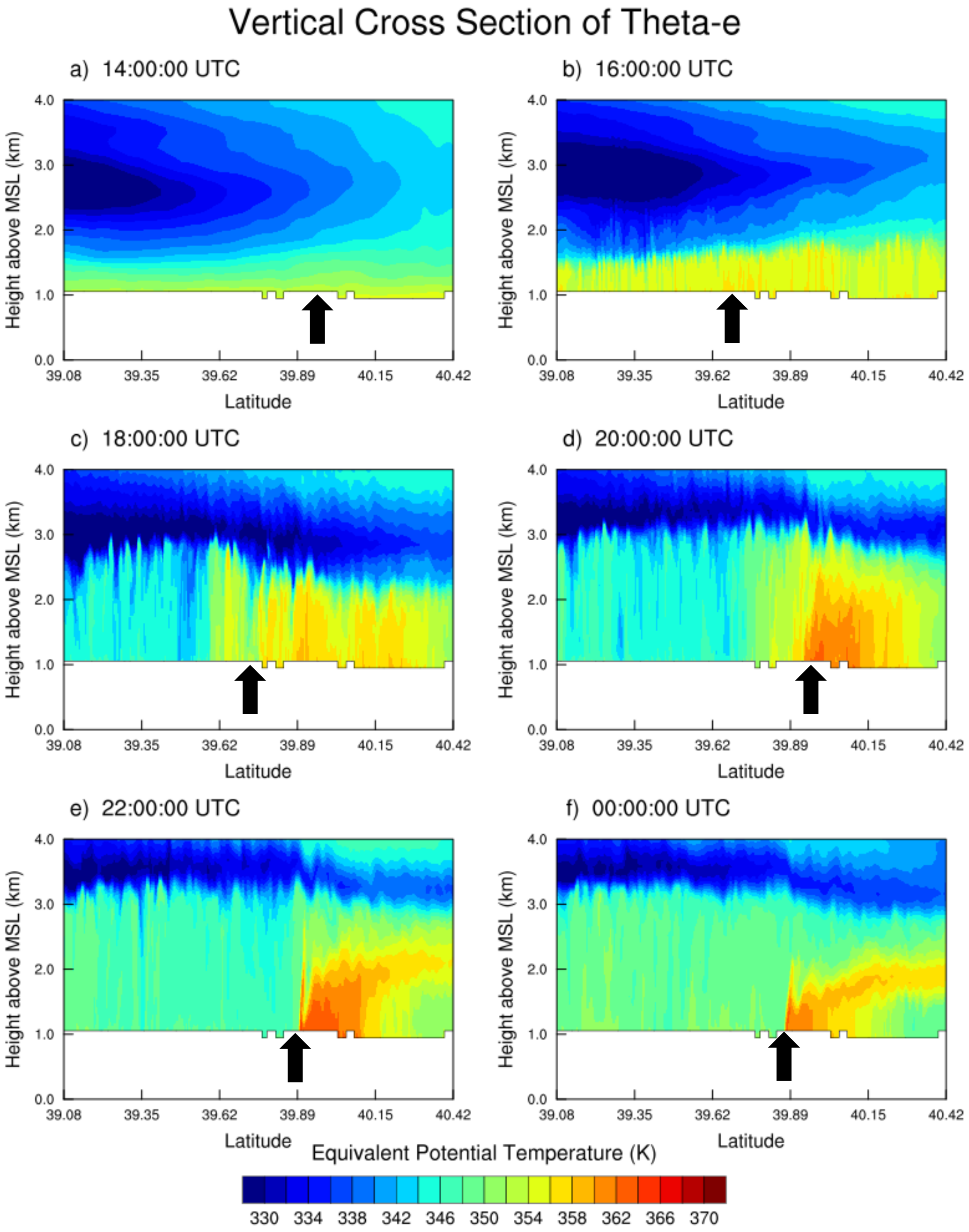

Figure 4.6: South-north vertical cross section of simulated θ_e (K). The approximate location of the cold front is indicated by the black arrow.

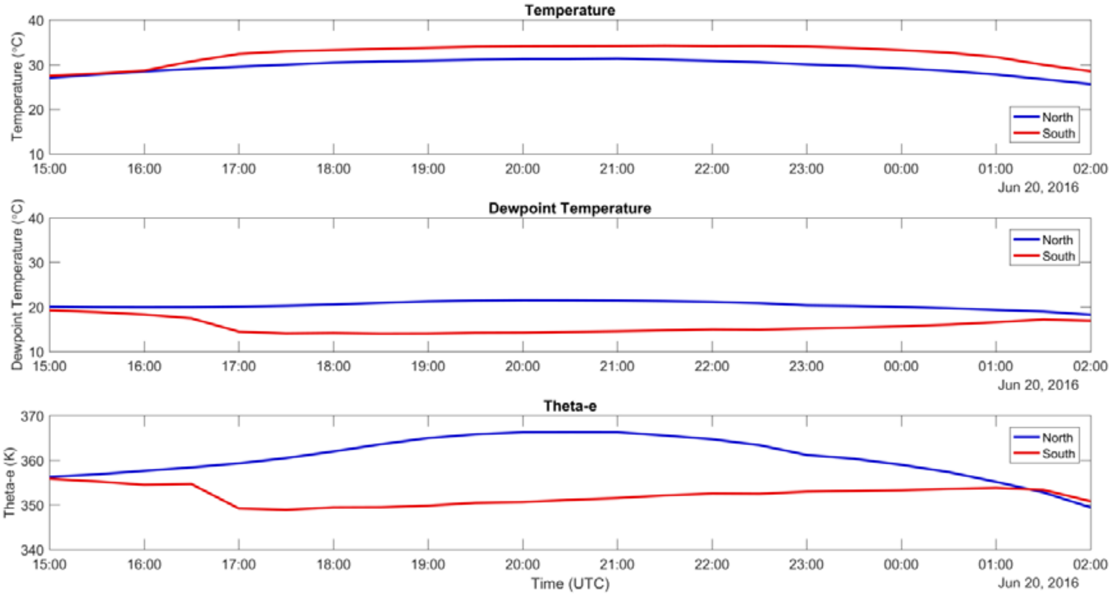

Figure 4.7: Area averaged 2-m temperature (°C), dewpoint temperature (°C), and θ_e (K). The blue line represents averages in the northern area and the red line represents the southern area.

Over the period from 1800 UTC to 2000 UTC, θ_e continued to increase north of the front (Figure 4.4d) with peak values increasing to 369 K. There was a clearly defined south-north gradient in temperature (Figure 4.1d), with a northeast-southwest gradient in dewpoint temperature across the domain (Figure 4.5d). θ_e at this time was highest where dewpoint temperature is highest (Figures 4.4d and 4.5d). During this period, the gradient in dewpoint temperature continued to increase along the cold front. This resulted in an increase of the θ_e gradient, to 0.83 K km^{-1}. However, as a consequence of the north-to-south temperature gradient, the θ_e gradient reversed 3-5 km north of the cold front, yielding θ_e values along the northern extent of the domain that were nearly identical to those in the warm sector. This 35 km wide zone of high θ_e north of the front is the MAHTE.

By 2200 UTC, further increases in the dewpoint temperature gradient across the cold front had yielded concomitant increases in the θ_e gradient, now reaching a maximum of 1.84 K km^{-1} (Figure 4.4). The highest values of θ_e at 2200 UTC were approximately 372 K, and were found directly along the cold side of the cold front. The overall width of the MAHTE at this point was approximately 30 km. As the afternoon progressed into the evening, the peak θ_e within the MAHTE decreased and the overall width of the MAHTE continued to contract (Figure 4.4f). The decrease in peak θ_e was due to a slight reduction in surface dewpoint temperature to the north of the front (Figure 4.5f), as well as a reduction in temperature across the entire domain (Figure 4.3f) due to decreased insolation.

Soundings from the model illustrate the vertical thermodynamic profile at a given point, allowing the diagnosis of potential explanations for MAHTE development; specifically, vertical stability and extent of vertical mixing. To be consistent with the methodology of the modified RAP soundings, the soundings within the warm environment were taken at a fixed location approximately where the RAP point soundings were obtained, while soundings in the MAHTE were taken in a location of the maximum θ_e along the same longitude of the surface transects (Figure 4.8). The model soundings at 2200 UTC (Figure 4.9) indicate in the warm environment that there is a well-mixed boundary layer up to approximately 725 mb, with a small inversion above the well mixed layer. Within the MAHTE, there is a shallow stable layer located at 850 hPa. Below this, dewpoint temperatures indicate a well-mixed boundary layer, while above this stable layer is a drier layer. Above this stable layer at the top of the well-mixed boundary layer, the MAHTE sounding profile begins to match the profile observed in the warm environment. This slight stable layer is likely arising from warm air advection as winds are southerly above the MAHTE, and could act to suppress mixing between the MAHTE mixed layer and the overlying elevated mixed layer. This suppression of vertical mixing would allow moisture content and θ_e within the MAHTE boundary layer to remain higher into the afternoon.

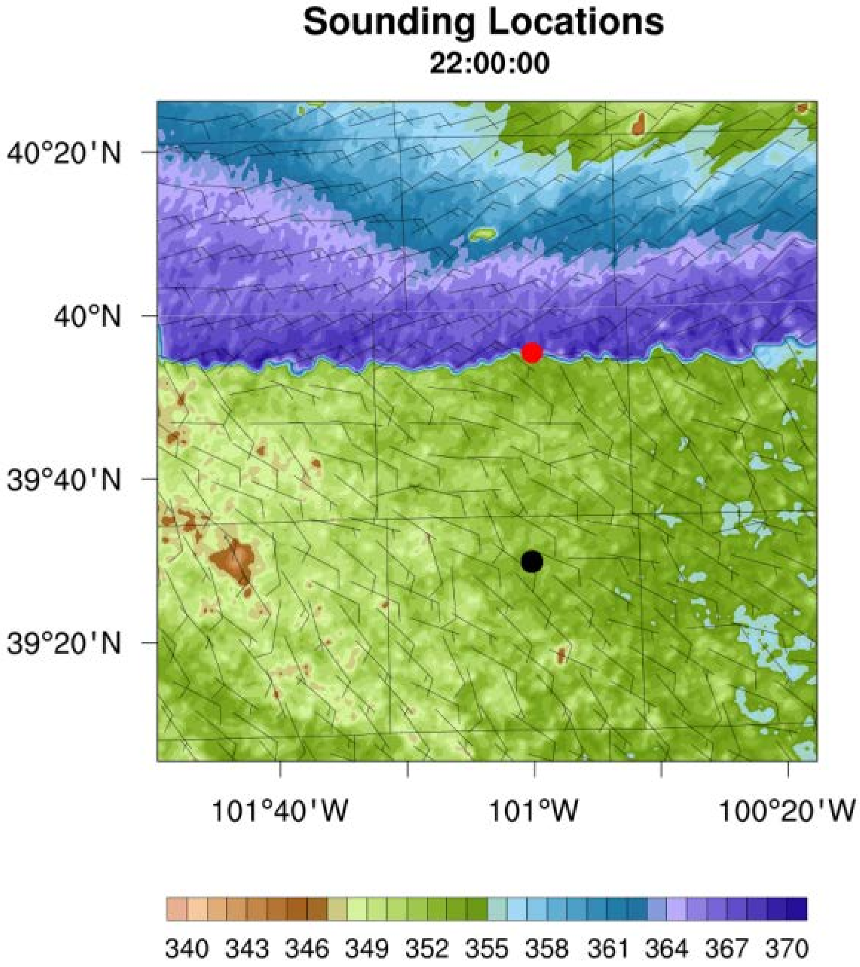

Figure 4.8: Locations of the soundings in the MAHTE (red dot) and warm environment (black dot).

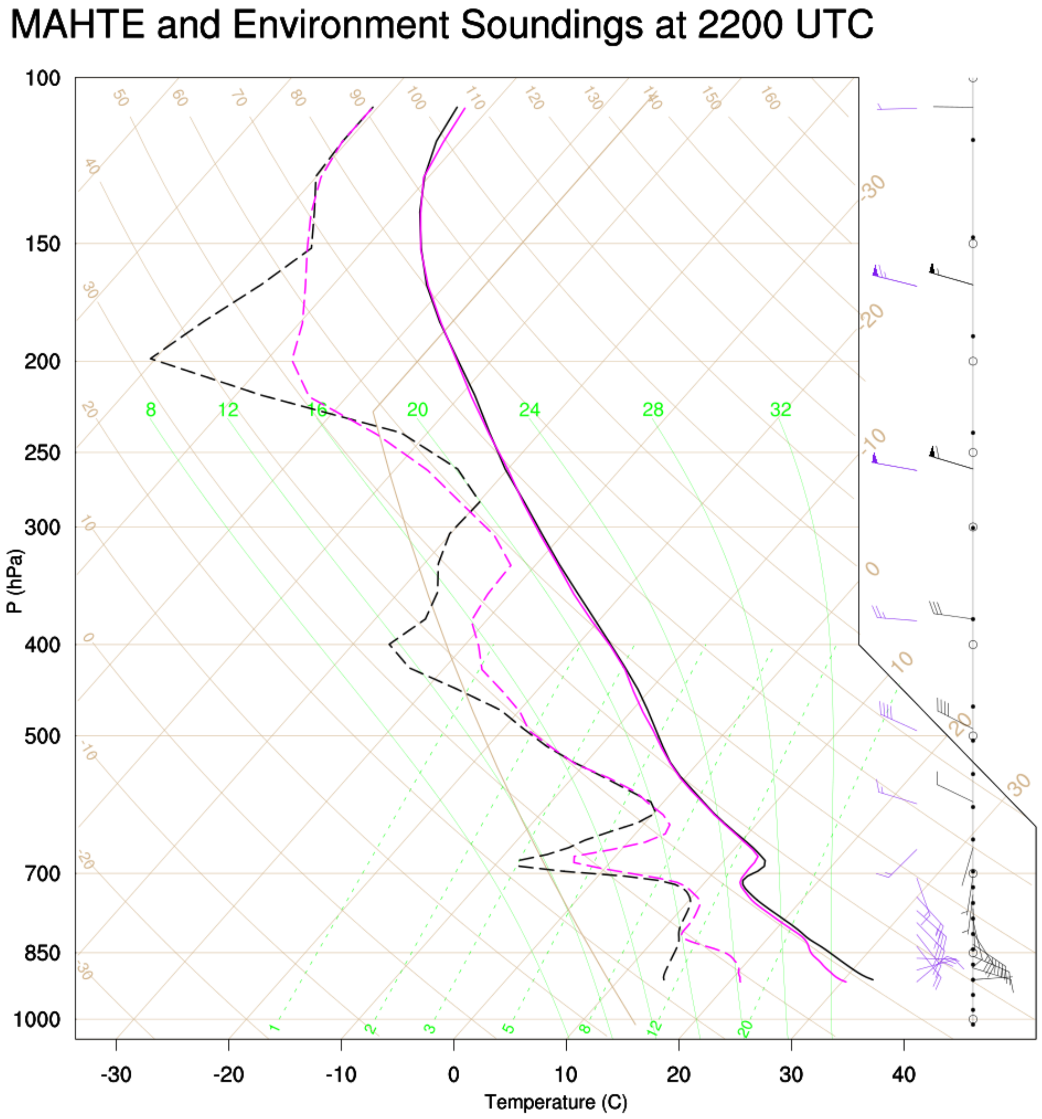

Figure 4.9: Soundings taken in the warm environment (black), in the MAHTE (magenta). Solid lines indicate temperature, dashed lines indicate dewpoint temperature.

Soundings derived from these simulations are generally consistent with the modified RAP soundings using near-surface observations. These modified soundings, discussed previously, showed that SBCAPE was significantly higher within the MAHTE compared to the warm environment, and the spatial distribution of most unstable convective available potential energy (MUCAPE) at the time of the highest θ_e in the simulations also reflects this (Figure 4.10). The most unstable parcel was used for these calculations of CAPE, which in these simulations were surface based parcels; therefore the MUCAPE calculated is equivalent to the SBCAPE. When the MAHTE had fully developed by 2200 UTC, MUCAPE approached 4000 J kg^{-1} directly on the cold side of the cold front (Figure 4.10a). With the observed increase of the gradients of dewpoint temperature and θ_e, there is a tight gradient in MUCAPE across the boundary, with MUCAPE below 1000 J kg^{-1} in the warm air mass. This illustrates that there was an approximate 3000 J kg^{-1} increase in MUCAPE in the MAHTE. This difference in MUCAPE is similar to differences observed with the modified RAP soundings discussed previously, despite the values of MUCAPE being lower both in the MAHTE and in the warm environment. Within the MAHTE, most unstable convective inhibition (MUCIN) decreased throughout the morning, reaching values between 0 J kg^{-1} and -25 J kg^{-1} by 2200 UTC when the MAHTE was mature (Figure 4.10b).

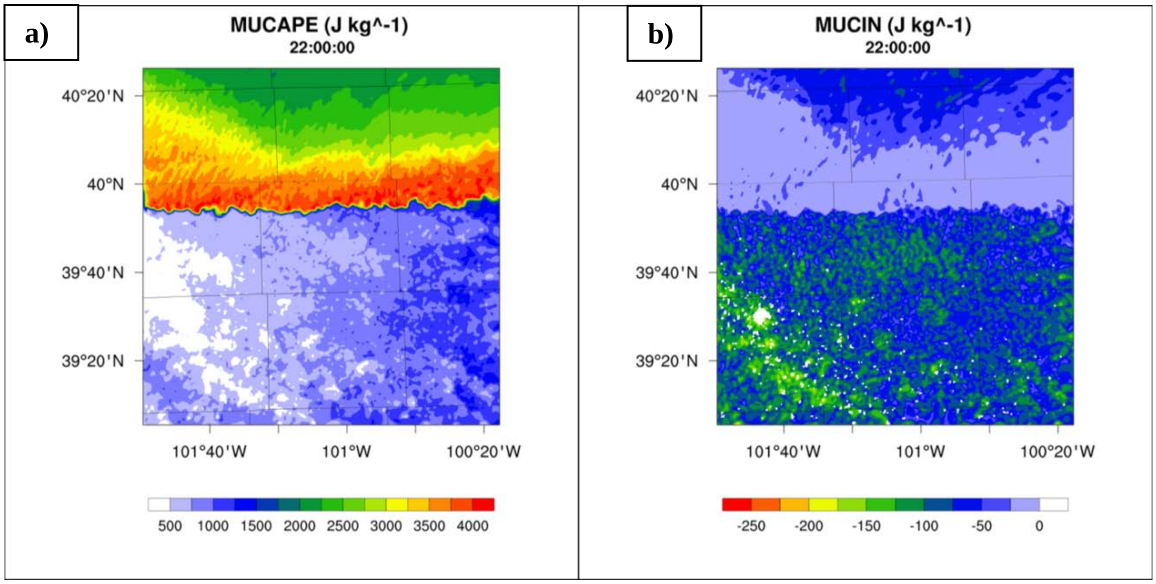

Figure 4.10: a) simulated MUCAPE and b) MUCIN at 22 UTC.

Chapter 5

Discussion of processes leading to MAHTE formation

To diagnose the mechanisms responsible for MAHTE formation, θ_e tendency must be evaluated. As discussed previously, θ_e changes primarily due to changes to temperature and atmospheric moisture. Because diabatic heating through insolation occurred nearly uniformly across the entire domain and because temperature advection should serve to decrease θ_e within the MAHTE, the primary mechanism(s) responsible for θ_e changes must be changes in moisture content. θ_e can change in a localized area through moisture fluxes from the surface, horizontal advection of θ_e which accounts for both moisture and temperature advection, and through vertical mixing. Each of these components will be examined here.

Increased surface moisture flux within the colder air mass attributable to stronger surface winds could increase atmospheric moisture (Yokoi et al. 2014). However, throughout the development stages of the MAHTE, 1800 – 2200 UTC, surface fluxes of moisture are slightly higher south of the front (Figure 5.1). This is due to the higher temperatures in the warmer air mass and similar wind speeds across the front. Due to uniformity in surface moisture flux across the domain for the duration of the simulation, this parameter alone cannot be responsible for maintaining moisture within the MAHTE.

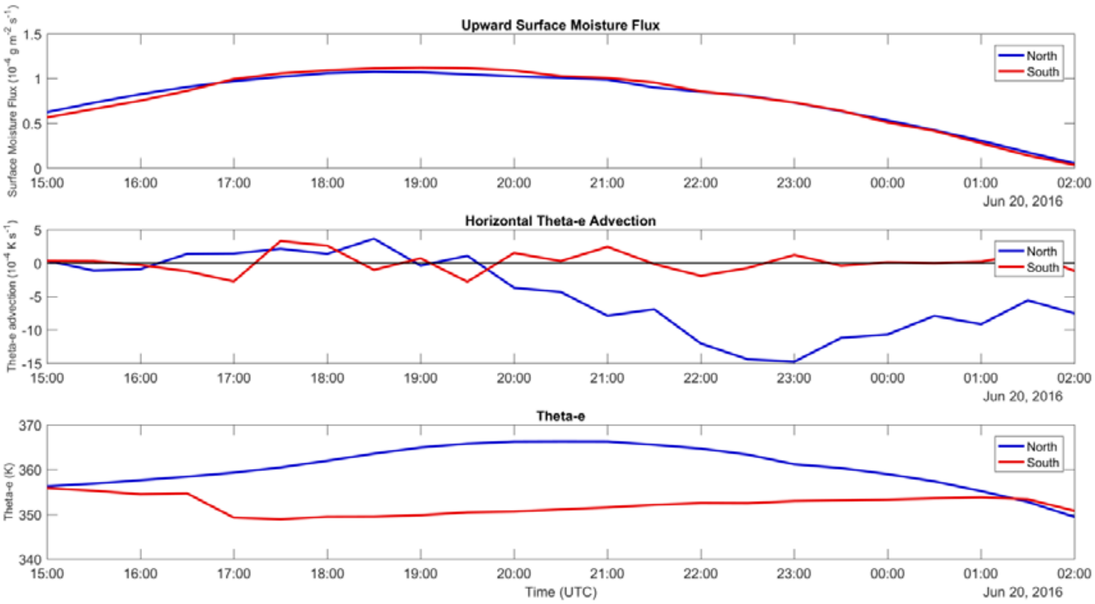

Figure 5.1: Area averaged upward surface moisture flux (10^{-4} g m^{-2} s^{-1}), horizontal θ_e advection (10^{-4} g kg^{-1} s^{-1}), and θ_e (K).

Another way that θ_e can change is through horizontal θ_e advection. Time series plots of average horizontal θ_e advection to the north and south of the front in Figure 5.1 show that horizontal θ_e advection is similar across the front during the formation stages of the MAHTE, with both areas having near zero horizontal θ_e advection. θ_e advection remains near zero throughout the simulation in the southern area, while advection becomes negative after 2200 UTC in the MAHTE area. This is due to the MAHTE progressing to the south, as well as due to the negative θ_e gradient to the north of the MAHTE moving into the area used for averaging. Ultimately, the lack of substantial differences in horizontal θ_e advection across the front during the time of MAHTE development means that that horizontal θ_e advection was not responsible for formation of the simulated MAHTE.

For differential vertical mixing to be important for MAHTE formation, there should be a difference in vertical velocity evolution across the cold front, resulting in a greater reduction in θ_e where vertical velocities are the strongest. The evolution of vertical cross sections of vertical velocity (Figure 5.2) illustrate that there is differential vertical mixing occurring across the boundary: vertical mixing throughout the morning and afternoon is stronger and deeper to the south of the cold front than the vertical mixing simulated to the north of the cold front (Figure 5.2). To quantify the impacts of differential vertical mixing on the development of the MAHTE, average vertical advection in a volume was calculated. This was done for a volume at the location of the 15 by 15 km areas used for all other averages (Figure 4.2), with a vertical dimension extending from the lowest model grid point to the 7th model grid point, corresponding to a height of approximately 375 m. This height was selected to roughly fill the stable boundary layer at the start of the simulations (as evident in Figure 4.6a) without extending above this. Initially at 1400 UTC, average vertical advection for both volumes was near zero (Figure 5.3), as vertical velocities were near zero (Figure 5.2a). By 1600 UTC, the boundary layer begins to transition into a convective boundary layer and vertical mixing begins to increase (Figure 5.2b). As the boundary layer deepens, lower θ_e air aloft is advected downward towards the surface, resulting in negative θ_e advection, strongest at 1630 UTC in the southern volume. This results in a lowering of average 2-m θ_e to the south of the cold front (Figure 4.4b), after which average vertical advection of θ_e to the south of the cold front becomes slightly positive once the boundary layer becomes well mixed. On contrast, vertical motions are suppressed within the MAHTE (Figure 5.2). Volume averaged vertical advection is near zero initially within the MAHTE, and then becomes positive likely due to the increasing θ_e at the surface with time (Figure 5.3). This illustrates that because the vertical depth of mixing is lower within the MAHTE, lower θ_e air aloft is never mixed throughout the boundary layer directly on the north side of the front, which allows moisture to remain constant and θ_e to rise within the MAHTE into the afternoon. Because of the difference in vertical advection of θ_e across the cold front, it is concluded that differential vertical advection is an important component in MAHTE formation.

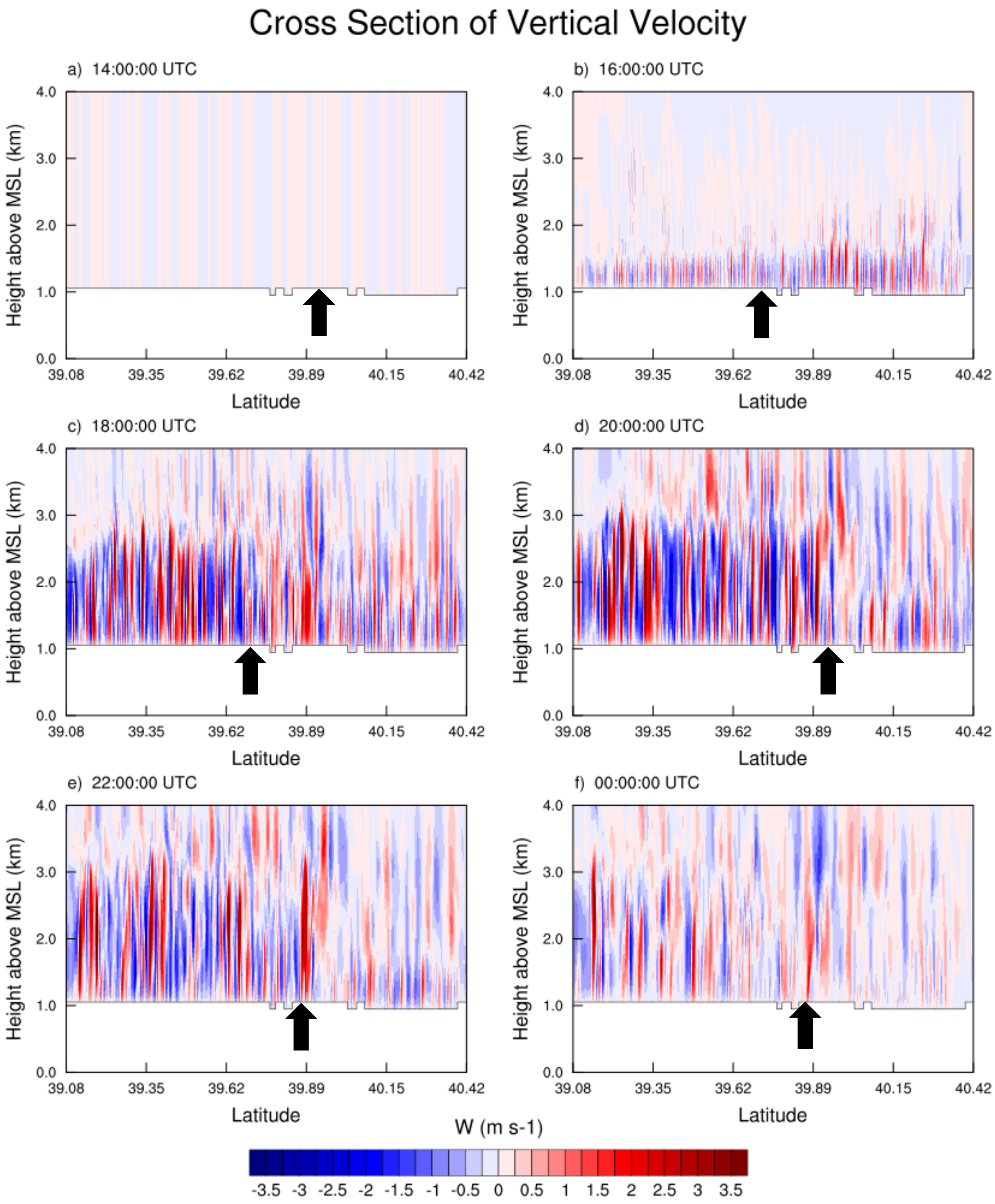

Figure 5.2: South-north vertical cross section of simulated vertical velocity (m s^{-1}). The approximate location of the front is indicated by the black arrow.

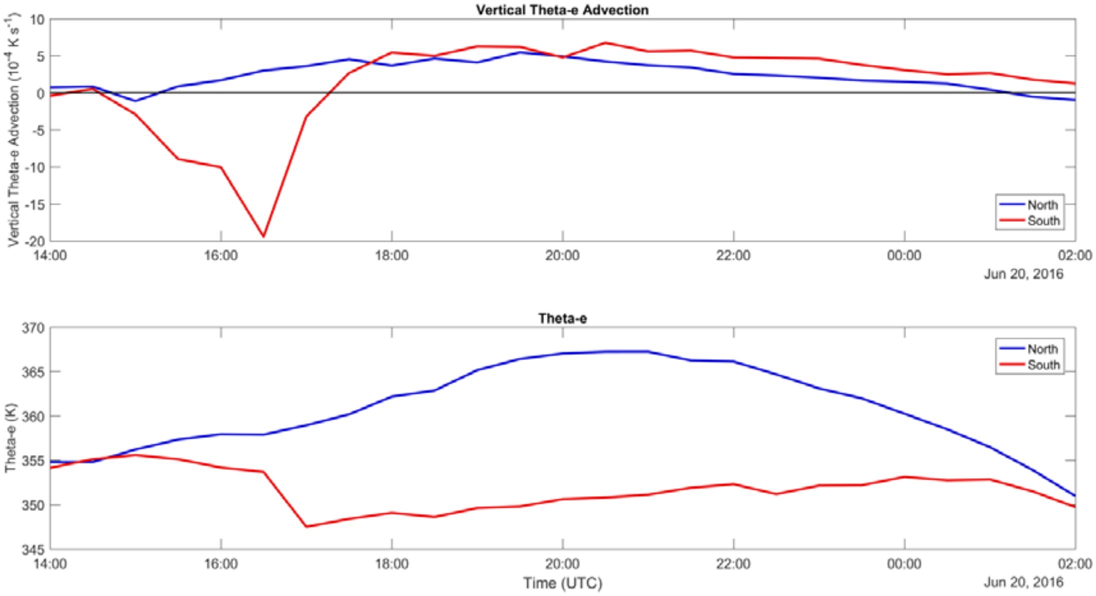

Figure 5.3: Average vertical advection of θ_e (10^{-4} K s^{-1}) and averaged 2-m θ_e (K).

Chapter 6

Summary and conclusions

A MAHTE along a synoptic cold front in northwest Kansas on 20 June 2016 was targeted for an investigation on MAHTE characteristics and formation. This case was modeled in WRF-ARW to examine the processes resulting in MAHTE formation and evolution, which cannot be deduced from observations alone. Observations showed that the MAHTE was approximately 40 km wide, which is wider than expected MAHTE width along an outflow boundary. The maximum value of θ_e was observed to be 372 K, decreasing steadily into the afternoon with each subsequent transect. The highest value of

θ_e was observed to be consistently 2 – 5 km on the cold side of the cold front, and was approximately 15 – 20 K higher than observations at the boundary and within the warm environment. The highest values of θ_e within the MAHTE were observed to be collocated with the greatest value of dewpoint temperature, in the region of quickly decreasing surface temperatures (within 10 km of the frontal boundary).

Simulations of this MAHTE accurately represented the formation of the MAHTE and its peak magnitude determined by the differences in θ_e and dewpoint temperatures between the warm air mass and the MAHTE. The greatest driver in MAHTE formation was differential vertical mixing across the boundary. Within the warmer air mass, vertical mixing was stronger and deeper than in the MAHTE, resulting in a decrease of the surface dewpoint and θ_e in the warm air mass, while suppressed vertical mixing within the MAHTE allowed dewpoint temperature to remain constant, while θ_e increased into the afternoon due to increasing insolation. Due to their similarities in magnitude across the boundary, horizontal θ_e advection and surface moisture fluxes cannot have resulted in a difference in the observed moisture, or the maintenance of moisture within the MAHTE, and thus are likely not responsible for the formation of the MAHTE. SBCAPE was approximately 3000 J kg^{-1} higher than observations in the warm air mass. This illustrates that MAHTE formation can have a significant impact on the convective environment over a localized area, which, if combined with a favorable backing of winds on the cool side of the boundary, could lead to an increased local severe thunderstorm potential.

Future work will include expanding research to include cases of MAHTE along thunderstorm outflow, similar to the cases referenced in the introduction. This will include a similar methodology as this study, taking both an observational and mesoscale modeling approach to determine the characteristics of these MAHTE, and the processes which lead to their formation and evolution. This will provide a more detailed knowledge base, which will help properly assess severe convective potential on a given day.

Bibliography

Banacos, P. C., and D. M. Schultz, 2005: The use of moisture flux convergence in forecasting convective initiation: Historical and operational perspectives. *Wea. Forecasting*, **20,** 351–366.

Bannon, P., 2002: Theoretical foundations for models of moist convection. *J. Atmos. Sci.*, **59,** 1967–1982.

Blumberg, W. G., K. T. Halbert, T. A. Supinie, P. T. Marsh, R. L. Thompson, and J. A. Hart, 2017: SHARPpy: An open source sounding analysis toolkit for the atmospheric sciences. *Bull. Amer. Meteor. Soc.* **98**, 1625–1636.

Bonan, G., 2016: *Ecological Climatology: Concepts and Applications*. Cambridge University Press, 692 pp.

Burghardt, B. J., C. Evans, and P. J. Roebber, 2014: Assessing the predictability of convection initiation in the high plains using an object-based approach. *Wea. Forecasting*, **29**, 403–418.

Charba, J., 1974: Application of gravity current model to analysis of squall-line gust front. *Mon. Wea. Rev.*, **102**, 140–156.

Chen, L., M. Zhuguo, and F. Xingang, 2012: A comparative study of two land surface schemes in WRF model over Eastern China. *J. of Tropical Meteor.*, **18**, 445-456.

Coniglio, M. C., J. Correia, P. T. Marsh, and F. Kong, 2013: Verification of convection-allowing WRF Model forecasts of the planetary boundary layer using sounding observations. *Wea. Forecasting*, **28**, 842–862.

Emanuel, K., 1994: *Atmospheric Convection*. Oxford University Press, 580 pp.

Engerer, N. A., D. J. Stensrud, and M. C. Coniglio, 2008: Surface characteristics of observed cold pools. *Mon. Wea. Rev.*, **136**, 4839–4849.

Gentine, P., A. Garelli, S.-B. Park, J. Nie, G. Torri, and Z. Kuang, 2016: Role of surface heat fluxes underneath cold pools, *Geophys. Res. Lett.*, 43, 874–883.

Gilmore, M. S. and L. J. Wicker, 2002: Influences of the local environment on supercell cloud-to-ground lightning, radar characteristics, and severe weather on 2 June 1995. *Mon. Wea. Rev*., **130**, 2349-2372.

Goody, R., 2000: Sources and sinks of climate entropy. *Quart. J. Roy. Meteor. Soc*, **126,** 1953–1970.

Grant, L. D. and S. C. van den Heever, 2015: Cold pool dissipation. *J. of Geophysical Research: Atmospheres*, **121 (3)**, 1138–1155.

Groenemeijer, P., U. Corsmeier, Ch. Kottmeier, 2010: The development of tornadic storms on the cold side of a front favoured by local enhancement of moisture and CAPE. *Atmospheric Research*, **100 (4)**, 765-781.

Guyer, J. L. and R. Ewald, 2004: Record hail event - examination of the Aurora, Nebraska supercell of 22 June 2003. Preprints, 22nd Conf. Severe Local Storms, Hyannis MA.

Hauf, T., and H. Höller, 1987: Entropy and potential temperature. *J. Atmos. Sci.*, **44,** 2887–2901.

Karan, H., 2014: Wind and thermodynamic profiler observations of a late-mature gust front. *J. Earth Syst. Sci.*, **123**, 161-165.

Langhans, W., D. M. Romps, 2015: The origin of water vapor rings in tropical oceanic cold pools. *Geophysical Research Letters*, **48 (18)**, 7825-7834.

Lowe, R. J., P. F. Linden, and J. W. Rottman, 2002: A laboratory study of the velocity structure in an intrusive gravity current. *J. Fluid Mech.*, **456**, 33-48.

Markowski, P., and Y. Richardson, 2010: *Mesoscale Meteorology in Midlatitudes*. Wiley-Blackwell, 407 pp.

Mlawer, E. J., S. J. Taubman, P. D. Brown, M. J. Iacono, and S. A. Clough, 1997: Radiative transfer for inhomogeneous atmosphere: RRTM, a validated correlated-k model for the long wave. *J. Geophys. Res.*, **102,** D14. 16663–16682.

Morrison, H., G. Thompson, and V. Tatarskii, 2009: Impact of cloud microphysics on the development of trailing stratiform precipitation in a simulated squall line: Comparison of one- and two-moment schemes. *Mon. Wea. Rev.*, **137**, 991–1007.

Okalebo, J., R. J. Oglesby, F. Song, K. Hubbard, K. Ayse, M. Hayes, and C. Hays, 2016: An Evaluation of the Community Land Model (Version 3.5) and Noah Land Surface Models for Temperature and Precipitation Over Nebraska (Central Great Plains): Implications for Agriculture in Simulations of Future Climate Change and Adaptation. *Climate Change Adaptation, Resilience and Hazards*. Springer International Publishing 21-34.

Pauluis, O., and I. M. Held, 2002: Entropy budget of an atmosphere in radiative–convective equilibrium. Part II: Latent heat transport and moist processes. *J. Atmos. Sci*, **59,** 140–149.

Peixoto, J. P., M. de Almeida, and A. Tomé, 1991: Entropy budget of the atmosphere. *J. Geophys. Res*, **96,** 10981–10988.

Rasmussen, E. N., S. Richardson, J. M. Straka, P. M. Markowski, and D. O. Blanchard, 2000: The association of significant tornadoes with a baroclinic boundary on 2 June 1995. *Mon. Wea. Rev*., **128 (1)**, 174-191.

Raymond, D. J., 2014: Sources and sinks of entropy in the atmosphere. *J. Adv. Model. Earth Syst.*, **5**, 755-763.

Riganti, C. J., and A. L. Houston, 2017: Rear-flank dynamics and thermodynamics in the 10 June 2010 Last Chance, Colorado supercell. *Mon. Wea. Rev*., **147 (7)**, 2487-2504.

Robinson, F. J., M. D. Patterson, and S. C. Sherwood, 2013: A numerical modeling study of the propagation of idealized sea-breeze density currents. *J. Atmos. Sci.*, **70**, 653–668.

Ross, A. N., A. M. Tompkins, and D. J. Parker, 2004: Simple models of the role of surface fluxes in convective cold pool evolution. *J. Atmos. Sci.*, **61**, 1582–1595.

Schlemmer, L., and C. Hohenegger, 2015: Modifications of the atmospheric moisture field as a result of cold-pool dynamics. *Quart. J. Roy. Meteor. Soc.* **142**, 30–42.

Seifert, A., and T. Heus, 2013: Large-eddy simulation of organized precipitating trade wind cumulus clouds. *Atmos. Chem. Phys. Discuss.*, **13**, 1855–1889.

Simpson, J. E., 1987: *Gravity Currents in the Environment and Laboratory*. Ellis Horwood Limited, 248 pp.

Skamarock, W. C., J. B. Klemp, J. Dudhia, D. O. Gill, D. M. Barker, M. G Duda, X.-Y. Huang, W. Wang, and J. G. Powers, 2008: A Description of the Advanced Research WRF Version 3. *NCAR Tech. Note NCAR/TN-475+STR*, 113 pp.

Skyllingstad, E. D., and S. P. de Szoeke, 2015: Cloud-resolving large-eddy simulation of tropical convective development and surface fluxes. *Mon. Wea. Rev.*, **143**, 2441–2458.

Stull, R., 2000: *Meteorology for Science and Engineers.* Brooks/Cole, 502 pp.

Tewari, M., F. Chen, W. Wang, J. Dudhia, M. A. LeMone, K. Mitchell, M. Ek, G. Gayno, J. Wegiel, and R. H. Cuenca, 2004: Implementation and verification of the unified NOAH land surface model in the WRF model. 20th Conference on Weather Analysis and Forecasting/16th Conference on Numerical Weather Prediction, pp. 11–15.

Tompkins, A. M., 2001: Organization of tropical convection in low vertical wind shears: the role of cold pools. *J. Atmos. Sci.*, **58 (13)**, 1650–1672.

Yokoi, S., M. Katsumata, and K. Yoneyama, 2014: Variability in surface meteorology and air-sea fluxes due to cumulus convective systems observed during CINDY/DYNAMO. *J. Geophys. Res. Atmos*., **119**, 2064–2078.

Young, G. S., S. M. Perugini, and C. W. Fairall, 1995: Convective wakes in the equatorial western Pacific during TOGA. *Mon. Wea. Rev.*, **123**, 110–123.

Wakimoto, R. M., H. Cai, and H. V. Murphey, 2004: The Superior, Nebraska, Supercell During BAMEX. *Bull. Amer. Meteor. Soc.*, **85**, 1095-1106.